

Structure of molten NaCl and the decay of the pair-correlations ^{EP}

Cite as: J. Chem. Phys. **157**, 094504 (2022); <https://doi.org/10.1063/5.0107620>

Submitted: 06 July 2022 • Accepted: 10 August 2022 • Published Online: 07 September 2022

Published open access through an agreement with JISC Collections

 Anita Zeidler,  Philip S. Salmon,  Takeshi Usuki, et al.

COLLECTIONS

 This paper was selected as an Editor's Pick



View Online



Export Citation



CrossMark

ARTICLES YOU MAY BE INTERESTED IN

[On the nature of the chemical bond in valence bond theory](#)

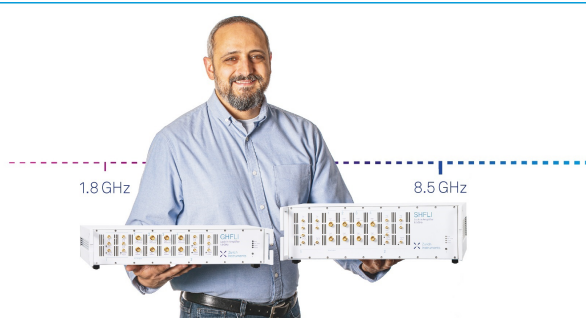
The Journal of Chemical Physics **157**, 090901 (2022); <https://doi.org/10.1063/5.0095953>

[Cross-correlation effects in the solution NMR spectra of near-equivalent spin-1/2 pairs](#)

The Journal of Chemical Physics **157**, 104112 (2022); <https://doi.org/10.1063/5.0107221>


[Homogeneous ice nucleation rates for mW and TIP4P/ICE models through Lattice Mold calculations](#)

The Journal of Chemical Physics **157**, 094503 (2022); <https://doi.org/10.1063/5.0101383>



Trailblazers. New

Meet the Lock-in Amplifiers that measure microwaves.

 Zurich Instruments [Find out more](#)

Structure of molten NaCl and the decay of the pair-correlations

Cite as: J. Chem. Phys. 157, 094504 (2022); doi: 10.1063/5.0107620

Submitted: 6 July 2022 • Accepted: 10 August 2022 •

Published Online: 7 September 2022



Anita Zeidler,¹  Philip S. Salmon,^{1,a)}  Takeshi Usuki,²  Shinji Kohara,³  Henry E. Fischer,⁴ 
and Mark Wilson⁵ 

AFFILIATIONS

¹ Department of Physics, University of Bath, Bath BA2 7AY, United Kingdom

² Department of Material and Biological Chemistry, Faculty of Science, Yamagata University, 1-4-12 Koshirakawa, Yamagata 990-8560, Japan

³ Research Center for Advanced Measurement and Characterization, National Institute for Materials Science (NIMS), Ibaraki 305-0047, Japan

⁴ Institut Laue Langevin, 71 Avenue des Martyrs, 38042 Grenoble Cedex 9, France

⁵ Department of Chemistry, Physical and Theoretical Chemistry Laboratory, University of Oxford, South Parks Road, Oxford OX1 3QZ, United Kingdom

^{a)} Author to whom correspondence should be addressed: p.s.salmon@bath.ac.uk

ABSTRACT

The structure of molten NaCl is investigated by combining neutron and x-ray diffraction with molecular dynamics simulations that employed interaction potentials with either rigid or polarizable ions. Special attention is paid to the asymptotic decay of the pair-correlation functions, which is related to the small- k behavior of the partial structure factors, where k denotes the magnitude of the scattering vector. The rigid-ion approach gives access to an effective restricted primitive model in which the anion and cation have equal but opposite charges and are otherwise identical. For this model, the decay of the pair-correlation functions is in qualitative agreement with simple theory. The polarizable ion approach gives a good account of the diffraction results and yields thermodynamic parameters (density, isothermal compressibility, Debye screening length, and heat capacity) in accord with experiment. The longest decay length for the partial pair-distribution functions is a factor of ≈ 2.5 times greater than the nearest-neighbor distance. The results are commensurate with the decay lengths found for the effective restricted primitive model, which are much shorter than those found in experiments on concentrated electrolytes or ionic liquids using surface force apparatus.

© 2022 Author(s). All article content, except where otherwise noted, is licensed under a Creative Commons Attribution (CC BY) license (<http://creativecommons.org/licenses/by/4.0/>). <https://doi.org/10.1063/5.0107620>

I. INTRODUCTION

Molten salts have enjoyed a resurgence of interest because of their potential applications as the thermal energy storage material in concentrated solar power plants,^{1–4} as the electrolyte in the so-called liquid-metal batteries for grid-energy storage, where the electrodes are made from liquid metals,^{5,6} and as the fuel and coolant system for next-generation nuclear-fission molten salt reactors.⁷ They also find applications as the flux in the refinement of molten aluminum⁸ and as the electrolyte in the processing of nuclear fuel^{9–11} or in the recovery of metals such as the rare-earth elements from scrap waste.¹¹

In order to predict the structure-related properties of a material, it is necessary to have an accurate model for describing the interactions between the atoms. Here, molten salts have long been used as a test bed for the development of these models because they are relatively simple ionic systems.^{12,13} Often, it is possible to measure the full set of partial structure factors via the method of neutron diffraction with isotope substitution,^{14–17} which delivers maximal information on the pair-correlation functions for testing the theoretical predictions. Such work has led to the incorporation of the energy terms associated with the ion polarization, leading to the so-called polarizable ion model (PIM).^{18–20} These polarization terms play an important role in accurately predicting the structure and properties

of the different phases.^{21,22} More recently, molten NaCl has been used as a test-bed system for the development of interatomic potentials via machine learning techniques.²³

The nature of the interatomic interactions also makes molten salts an attractive proposition for exploring the asymptotic behavior of the pair-correlation functions, and thereby testing the predictions of simple theories that should also apply to inhomogeneous fluids at large distances from an interface.^{24,25} In the case of concentrated electrolytes and ionic liquids, such theories have been called into question: The decay of the pair-correlation functions found from experiment^{26–28} is much slower than that expected from simple theories based, e.g., on the restricted primitive model (RPM) in which equally sized hard-sphere ions are embedded in a uniform dielectric medium. In concentrated electrolytes or ionic liquids, the discrepancy between the measured and predicted decay lengths is typically an order of magnitude or more.²⁹

We have therefore been motivated to re-examine the structure of the archetypal molten salt NaCl by combining state-of-the-art neutron and x-ray diffraction experiments with molecular dynamics simulations. The objective is to obtain accurate information at the partial pair-correlation function level to provide a comparison with previous neutron¹⁶ and x-ray^{30,31} diffraction results and to test, *inter alia*, the long-ranged decay of the pair-correlation functions and how it relates to simple theory.^{24,25}

This paper is organized as follows: The diffraction theory is outlined in Sec. II for a molten salt of arbitrary composition in order to retain a general notation for the corrections that are required to calculate the asymptotic behavior of the pair-correlation functions for simulations on a system of finite size. The diffraction experiments are described in Sec. III. The model potentials are outlined in Sec. IV, where a PIM and two rigid-ion models (RIMs) are considered in order to probe the effect of different energy terms on the melt structure. The molecular dynamics simulations are described in Sec. V. The results are presented in Sec. VI using both the Faber–Ziman (FZ)³² and Bhatia–Thornton (BT)³³ representations of the pair-correlation functions. The FZ representation emphasizes the contributions to the structure from the distribution of ion–ion pairs. The BT representation emphasizes the contributions to the structure from the number density and concentration fluctuations, which relate more readily to the thermodynamic properties of the melt. The results are discussed in Sec. VII by reference to the thermodynamic properties of the melt, the dependence of the structure on the interatomic potentials, and the decay of the pair-correlation functions at large- r values, where r is a distance in real-space. Conclusions are drawn in Sec. IX.

II. THEORY

The total structure factor $F(k)$ measured in a neutron or x-ray diffraction experiment on a molten salt, such as MX or MX₂, where M and X denote a cation and anion, respectively, can be decomposed into its contributions from the pair-correlation functions describing the atomic species according to³⁴

$$F(k) = \sum_{\alpha} \sum_{\beta} c_{\alpha} c_{\beta} w_{\alpha}(k) w_{\beta}(k) [S_{\alpha\beta}^{\text{FZ}}(k) - 1], \quad (1)$$

where c_{α} denotes the atomic fraction of chemical species α (M or X), $w_{\alpha}(k)$ represents either the k -dependent x-ray form factor $f_{\alpha}(k)$ or

the k -independent coherent neutron scattering length b_{α} of chemical species α , and $S_{\alpha\beta}^{\text{FZ}}(k)$ is the FZ partial structure factor for chemical species α and β . In an x-ray diffraction experiment, Eq. (1) is usually re-written as

$$S_X(k) = 1 + \frac{F(k)}{\langle w(k) \rangle^2}, \quad (2)$$

where $\langle w(k) \rangle = c_M w_M(k) + c_X w_X(k)$.

In experiment, the partial pair-distribution functions $g_{\alpha\beta}(r)$ are obtained from the Fourier transform,

$$g_{\alpha\beta}(r) = 1 + \frac{1}{2\pi^2 n_0 r} \int_0^{\infty} dk k [S_{\alpha\beta}^{\text{FZ}}(k) - 1] \sin(kr), \quad (3)$$

where $n_0 = N/V$ is the ion number density, N is the total number of ions, and V is the volume. In simulation, the $g_{\alpha\beta}(r)$ functions are calculated from direct knowledge of the atomic positions. The mean coordination number of atoms of type β , contained within a volume defined by two concentric spheres of radii r_{\min} and r_{\max} centered on an atom of type α , is given by

$$\bar{r}_{\alpha}^{\beta} = 4\pi n_0 c_{\beta} \int_{r_{\min}}^{r_{\max}} dr r^2 g_{\alpha\beta}(r). \quad (4)$$

The total structure factor can also be decomposed into its contributions from the number density and concentration fluctuations³³ such that Eq. (1) is re-written as

$$F(k) = \langle w(k) \rangle^2 [S_{\text{NN}}^{\text{BT}}(k) - 1] + c_M c_X [w_M(k) - w_X(k)]^2 \{ [S_{\text{CC}}^{\text{BT}}/c_M c_X] - 1 \} + 2\langle w(k) \rangle [w_M(k) - w_X(k)] S_{\text{NC}}^{\text{BT}}(k), \quad (5)$$

where $S_{\text{NN}}^{\text{BT}}(k)$, $S_{\text{CC}}^{\text{BT}}(k)$, and $S_{\text{NC}}^{\text{BT}}(k)$ represent the BT number–number, concentration–concentration, and number–concentration partial structure factors, respectively. The FZ and BT partial structure factors are related by the expressions

$$S_{\text{NN}}^{\text{BT}}(k) = c_M^2 S_{\text{MM}}^{\text{FZ}}(k) + c_X^2 S_{\text{XX}}^{\text{FZ}}(k) + 2c_M c_X S_{\text{MX}}^{\text{FZ}}(k), \quad (6)$$

$$S_{\text{CC}}^{\text{BT}}(k) = c_M c_X \{ 1 + c_M c_X [S_{\text{MM}}^{\text{FZ}}(k) + S_{\text{XX}}^{\text{FZ}}(k) - 2S_{\text{MX}}^{\text{FZ}}(k)] \}, \quad (7)$$

and

$$S_{\text{NC}}^{\text{BT}}(k) = c_M c_X \{ c_M [S_{\text{MM}}^{\text{FZ}}(k) - S_{\text{MX}}^{\text{FZ}}(k)] - c_X [S_{\text{XX}}^{\text{FZ}}(k) - S_{\text{MX}}^{\text{FZ}}(k)] \}. \quad (8)$$

The low- k limits of the BT partial structure factors are related to key thermodynamic properties according to the equations

$$\begin{aligned} S_{\text{NN}}^{\text{BT}}(0) &= n_0 k_B T \chi_T + \delta^2 S_{\text{CC}}(0), \\ S_{\text{CC}}^{\text{BT}}(0) &= k_B T / (\partial^2 G / \partial c_M^2)_{T,p,N}, \\ S_{\text{NC}}^{\text{BT}}(0) &= -\delta S_{\text{CC}}(0), \end{aligned} \quad (9)$$

where T is the absolute temperature, p is the pressure, k_B is the Boltzmann constant, χ_T is the isothermal compressibility, G is the Gibbs free energy, and the dilation factor $\delta = n_0(v_M - v_X)$, where v_α is the partial molar volume per particle of chemical species α .

For an ionic system, the charge-charge partial structure factor $S_{ZZ}(k) = S_{CC}^{BT}(k)/c_M c_X$ satisfies the Stillinger-Lovett³⁵ conditions (i) $S_{ZZ}(0) = 0$, which expresses charge neutrality, and (ii) $S_{ZZ}(k) = \Lambda_D^2 k^2$ in the small- k region, where Λ_D is the Debye screening length given by

$$\Lambda_D^{-2} = \frac{4\pi n_0}{k_B T \epsilon} \sum_{\alpha} c_{\alpha} (Z_{\alpha} e)^2, \quad (10)$$

where $\epsilon \equiv 4\pi\epsilon_0\epsilon_r$, ϵ_r is the dimensionless relative dielectric constant, ϵ_0 is the vacuum permittivity, and $Z_{\alpha}e$ is the charge on ion α .³⁶ The Debye screening length is a consequence of requiring perfect screening in the long wavelength limit as $k \rightarrow 0$.^{37,38} Hence, $S_{CC}^{BT}(0) = S_{NC}^{BT}(0) = 0$ and $S_{NN}^{BT}(0) = n_0 k_B T \chi_T$.

The number-number partial pair-distribution function is given by the Fourier transform

$$g_{NN}^{BT}(r) - 1 = \frac{1}{2\pi^2 n_0 r} \int_0^{\infty} dk k [S_{NN}^{BT}(k) - 1] \sin(kr). \quad (11)$$

Equivalent expressions relate the concentration-concentration partial pair-distribution function $g_{CC}^{BT}(r)$ to $[S_{CC}^{BT}(k)/c_M c_X - 1]$ and the number-concentration partial pair-distribution function $g_{NC}^{BT}(r)$ to $S_{NC}^{BT}(k)/c_M c_X$.

III. EXPERIMENT

A. Neutron diffraction

The samples investigated by neutron diffraction were Na^{35}Cl (99% enrichment, Sigma-Aldrich), $\text{Na}^{\text{nat}}\text{Cl}$ (99.999%, Alfa Aesar), $\text{Na}^{\text{mix}}\text{Cl}$, and Na^{37}Cl (95% enrichment, Sigma-Aldrich), where nat denotes the natural isotopic abundance of chlorine and mix denotes a 50:50 mixture of ^{35}Cl and ^{37}Cl . The samples were loaded into cylindrical silica ampoules of inner diameter 5.0(2) mm and wall thickness 1.00(5) mm that had been cleaned using a 48 wt % solution of hydrofluoric acid, rinsed using water and then acetone, and baked dry under vacuum. The ampoules were sealed under a vacuum of 0.8×10^{-5} Torr. The coherent neutron scattering lengths, taking into account the isotopic enrichment, are $b_{\text{Na}} = 3.63(2)$ fm, $b_{^{35}\text{Cl}} = 11.56(2)$ fm, $b_{\text{natCl}} = 9.5770(8)$ fm, $b_{\text{mixCl}} = 7.36(2)$ fm, and $b_{^{37}\text{Cl}} = 3.51(6)$ fm.³⁹

The neutron diffraction experiment was performed using the instrument D4c at the Institut Laue-Langevin (ILL) with an incident wavelength of 0.6956(1) Å.⁴⁰ A vanadium furnace was used with a heating element of diameter 17 mm and wall thickness 0.1 mm, together with a heat shield of diameter 25 mm and wall thickness 0.04 mm. Diffraction patterns were measured at 1093(5) K for each sample in its container in the furnace, an empty container in the furnace, and the empty furnace. Diffraction patterns were also measured at room temperature for the empty furnace, a cylindrical vanadium rod of diameter 6.37(1) mm in the furnace for normalization purposes, and a rod of neutron absorbing cadmium (of dimensions comparable to the sample) in the furnace to account for

the effect of the sample self-shielding on the background count-rate at small scattering angles.⁴¹

Each diffraction pattern was built up from the intensities measured for the different detector groups. These intensities were saved at regular intervals to check for the stability of the experimental setup.⁴² For the $\text{Na}^{\text{mix}}\text{Cl}$ and Na^{37}Cl samples, the diffraction patterns showed the emergence of Bragg peaks, the most prominent at $k \approx 1.5 \text{ \AA}^{-1}$, which grew slowly with time as the sample began to react with its silica container.⁴³ This reaction resulted from contamination of the Na^{37}Cl sample and led to cracked containers when the melt was cooled to room temperature.⁴⁴ Water is a possible impurity,⁴⁵ but the characteristic shape associated with inelastic scattering from light hydrogen, to which neutron diffraction is particularly sensitive because of the large incoherent scattering cross section of light hydrogen,³⁴ was not observed in the diffraction patterns.

The data corrections followed a standard procedure.^{46,47} The number density recommended by Janz,⁴⁸ i.e., $n_0 = 0.03186(1) \text{ \AA}^{-3}$ at 1093 K,⁴⁹ was used in the data analysis. The Bragg peaks in the structure factors measured for the $\text{Na}^{\text{mix}}\text{Cl}$ and Na^{37}Cl samples were eliminated by taking the difference function

$$\Delta F(k) = {}^{\text{mix}}F(k) - {}^{37}F(k) \quad (12)$$

with $x = 0.9$.⁴³

B. X-ray diffraction

The x-ray diffraction experiment was performed using the beamline BL04B2 at SPring-8 with an incident energy of 61.65 keV corresponding to the (220) planes of a silicon monochromator.⁵⁰ The sample of $\text{Na}^{\text{nat}}\text{Cl}$ (99.999%, Alfa Aesar) was loaded into a cylindrical silica capillary tube of inner diameter 1.00(1) mm and wall thickness 1.00(5) mm, which had been cleaned using a 48 wt % solution of hydrofluoric acid, rinsed using water and then acetone, and baked dry under vacuum. The tube was sealed under a vacuum of 1.5×10^{-5} Torr. A vacuum bell jar was used to avoid air scattering, and the diffracted x rays were collected using a Ge solid-state detector. Diffraction patterns were measured at 1091(1) K for the sample in its container and an empty container. The x-ray data analysis procedure followed the method described elsewhere⁵⁰ using ion form factors⁵¹ and the Compton scattering correction taken from Refs. 52 and 53.

C. Partial structure factors

The measured functions are related to the FZ partial structure factors according to the equation

$$\begin{pmatrix} \Delta F(k) \\ {}^{\text{nat}}F(k) \\ {}^{35}F(k) \\ S_X(k) \end{pmatrix} = \begin{pmatrix} a_{11} & a_{12} & a_{13} \\ a_{21} & a_{22} & a_{23} \\ a_{31} & a_{32} & a_{33} \\ a_{41} & a_{42} & a_{43} \end{pmatrix} \begin{pmatrix} S_{\text{NaNa}}^{\text{FZ}}(k) - 1 \\ S_{\text{NaCl}}^{\text{FZ}}(k) - 1 \\ S_{\text{ClCl}}^{\text{FZ}}(k) - 1 \end{pmatrix}, \quad (13)$$

where the matrix elements are given by $a_{11} = (1-x)c_{\text{Na}}^2 b_{\text{Na}}^2$, $a_{12} = 2c_{\text{Na}}c_{\text{Cl}}b_{\text{Na}}(b_{\text{mixCl}} - xb_{^{37}\text{Cl}})$, $a_{13} = c_{\text{Cl}}^2(b_{\text{mixCl}}^2 - xb_{^{37}\text{Cl}}^2)$, $a_{21} = a_{31} = c_{\text{Na}}^2 b_{\text{Na}}^2$, $a_{22} = 2c_{\text{Na}}c_{\text{Cl}}b_{\text{Na}}b_{\text{natCl}}$, $a_{23} = c_{\text{Cl}}^2 b_{\text{natCl}}^2$, $a_{32} = 2c_{\text{Na}}c_{\text{Cl}}b_{\text{Na}}b_{^{35}\text{Cl}}$,

$a_{33} = c_{\text{Cl}}^2 b_{35\text{Cl}}^2$, $a_{41} = c_{\text{Na}}^2 f_{\text{Na}}(k)^2 / \langle f(k) \rangle^2$, $a_{42} = 2c_{\text{Na}} c_{\text{Cl}} f_{\text{Na}}(k) f_{\text{Cl}}(k) / \langle f(k) \rangle^2$, and $a_{43} = c_{\text{Cl}}^2 f_{\text{Cl}}(k)^2 / \langle f(k) \rangle^2$. Equation (13) can be rewritten as

$$\mathbf{F} = \mathbf{W}\mathbf{S}, \quad (14)$$

where \mathbf{F} is the column vector for the total structure factors, \mathbf{S} is the column vector for the partial structure factors, and \mathbf{W} is the $m \times n$ weighting factor matrix (m rows and n columns) with $m > n$ and rank equal to n . \mathbf{W} contains k -dependent matrix elements that originate from the x-ray form factors. The notation of Eq. (14) can also be used to relate \mathbf{F} to a column vector \mathbf{S} representing the BT partial structure factors $S_{IJ}^{\text{BT}}(k)$ ($I, J = \text{N, C}$).

A unique \mathbf{S} can be found by using singular value decomposition (SVD) to solve the least squares problem in which the two-norm $\|\mathbf{r}\|_2$ of the residual vector $\mathbf{r} = \mathbf{F} - \mathbf{W}\mathbf{S}$ is minimized.^{54,55} The weighting factor matrix can be written as $\mathbf{W} = \mathbf{U}\mathbf{\Sigma}\mathbf{V}^T$, where \mathbf{U} is an $m \times n$ orthogonal matrix, $\mathbf{\Sigma}$ is an $n \times n$ diagonal matrix with main diagonal elements $\sigma_1 \geq \sigma_2 \geq \dots \geq \sigma_n > 0$ known as the singular values, and \mathbf{V}^T is the transpose of an $n \times n$ orthogonal matrix \mathbf{V} . The least squares solution to Eq. (14) is then given by

$$\mathbf{S} = \sum_{l=1}^n \frac{(\mathbf{U}_l \cdot \mathbf{F})}{\sigma_l} \mathbf{V}_l, \quad (15)$$

where the vectors \mathbf{U}_l and \mathbf{V}_l represent the l th columns of the matrices \mathbf{U} and \mathbf{V} , respectively. If \mathbf{F} is subjected to an uncertainty $\delta\mathbf{F}$, then, the corresponding uncertainty $\delta\mathbf{S}$ on \mathbf{S} is given by

$$\delta\mathbf{S} = \sum_{l=1}^n \frac{(\mathbf{U}_l \cdot \delta\mathbf{F})}{\sigma_l} \mathbf{V}_l. \quad (16)$$

Figure 1 shows the k -dependence of the singular values σ_l ($l = 1, 2$ or 3) for the FZ and BT representations of the partial structure factors. In each case, σ_3 is much smaller than the other terms, which indicates that \mathbf{S} will be most sensitive to the uncertainty associated with the $l = 3$ term. In the FZ representation, successive components in the column vector $\mathbf{V}_3 = [0.877 \ -0.437 \ 0.199]^T$ correspond to the NaNa, NaCl, and ClCl partial structure factors, respectively, where the values are typical and correspond to $k = 0$. Thus, an uncertainty $\delta\mathbf{F}$ will lead to errors in the NaNa and ClCl partial structure factors that have an opposite sign to the error in the NaCl partial structure factor. In addition, the NaNa and ClCl partial structure factors will be the most and least sensitive to $\delta\mathbf{F}$, respectively. Similarly, in the Bhatia–Thornton representation, σ_3 is again much smaller than the other singular values. Successive components in the column vector $\mathbf{V}_3 = [-0.100 \ -0.980 \ -0.169]^T$ correspond to the NN, CC, and NC partial structure factors, respectively, where the values are typical and correspond to $k = 0$. Thus, an uncertainty $\delta\mathbf{F}$ will lead to an error that has the same sign for all the partial structure factors. The CC and NN partial structures factor will be the most and least sensitive to $\delta\mathbf{F}$, respectively.

The two-norm condition (or Turing) number of the weighting factor matrix is given by $\kappa_2 = \sigma_1/\sigma_n$, where σ_1 and σ_n are the largest and smallest singular values of \mathbf{W} , respectively. It follows that $\kappa_2 \geq 1$, where a value near to unity indicates a well conditioned

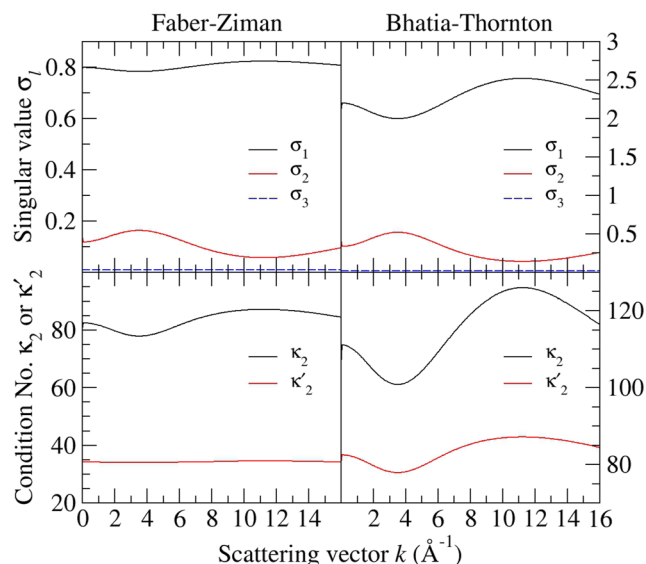


FIG. 1. The k -dependence of the singular values σ_l ($l = 1, 2$ or 3) and the condition numbers κ_2 and κ'_2 for the FZ (left column) and BT (right column) solutions to Eq. (14).

matrix. Sometimes, the two-norm condition number κ'_2 for the normalized matrix \mathbf{W}' is also quoted.^{54,55} Figure 1 shows the k -dependence of these condition numbers for the FZ and BT partial structure factors. The measured datasets are more favorable for extracting the $S_{\alpha\beta}^{\text{FZ}}(k)$ than the $S_{IJ}^{\text{BT}}(k)$ functions.

We note that the partial structure factors of this work were obtained from direct inversion of the measured k -space functions, without the application of any constraints, and therefore reflect the statistical error on those functions. It was checked that the extracted BT partial structure factors satisfy the inequality relations $S_{\text{NN}}^{\text{BT}}(k) \geq 0$, $S_{\text{CC}}^{\text{BT}}(k) \geq 0$, and $S_{\text{NN}}^{\text{BT}}(k)S_{\text{CC}}^{\text{BT}}(k) \geq S_{\text{NC}}^{\text{BT}}(k)^2$ within the experimental error, which originate from the need for the intensity measured in a diffraction experiment to be either zero or positive. Unlike previous work on molten NaCl,^{15,16} the partial structure factors were not obtained from an iterative procedure in which smoothed functions were extracted from the measured datasets via the application of physical constraints. These smoothed functions do not reflect a substantial statistical error on the measured diffraction patterns.¹⁵

IV. MODEL POTENTIALS

The potential energy between two ions labeled i and j with charges q_i and q_j , separated by the distance r_{ij} , can be expressed as

$$U_{\text{tot}}(r_{ij}) = U_{\text{sr}}(r_{ij}) + U_{\text{Coul}}(r_{ij}). \quad (17)$$

The short-ranged part was represented by a modified Born–Mayer⁵⁶ potential (see Ref. 12 and references therein) where, in atomic units,

$$U_{\text{sr}}(r_{ij}) = B_{ij}e^{-a_{ij}r_{ij}} - \sum_{n=6,8} \frac{C_{ij}^n}{r_{ij}^n} f_n(r_{ij}), \quad (18)$$

B_{ij} and a_{ij} are parameters controlling the ionic radius and the rate of decay of the repulsive wall, respectively, C_{ij}^n are dispersion parameters, and $\tilde{f}_n(r_{ij})$ are damping functions. The latter account for the loss of asymptotic behavior in the dispersion interactions at short range,⁵⁷ are of the form suggested by Tang and Toennies,⁵⁸ and are controlled by the parameters \tilde{b}_6^{ij} and \tilde{b}_8^{ij} . Traditionally, many-body polarization effects are incorporated using a shell model,⁵⁹ which is a mechanical representation of the dipolar charge displacement, composed of a charged shell connected by an harmonic spring to a charged core.^{12,60} In the PIM, the charge-charge Coulomb potential is also augmented with a description of ion polarization that takes a many-body character, but at the simplest level of a dipolar model, the induced dipoles μ_i are incorporated as point moments.¹⁹ In atomic units, the Coulomb (electrostatic) interaction is then given by

$$U_{\text{Coul}}(r_{ij}) = q_i T q_j + (q_i T_{\alpha\beta} \mu_{j,\alpha} - q_j T_{\alpha\beta} \mu_{i,\alpha}) [1 - \tilde{g}_{ij}(r_{ij})] - \mu_{i,\alpha} T_{\alpha\beta} \mu_{j,\beta} + k_i \mu_i^2, \quad (19)$$

where the charge $q_i = +1$ for Na^+ or $q_i = -1$ for Cl^- , $T = 1/r_{ij}$, and the interaction tensor $T_{\alpha\beta\dots} = \nabla_\alpha \nabla_\beta \dots (r_{ij})^{-1}$, where $\{\alpha, \beta\} = \{x, y, z\}$.⁵⁷ The first three terms represent the charge-charge, charge-dipole and dipole-dipole interactions. The fourth term represents the polarization energy, where $k_i = 1/2\alpha_i$ and α_i is the dipole polarizability of species i . The functions $\tilde{g}_{ij}(r_{ij})$ control the short-ranged contributions to the induced dipoles (see, for example, Refs. 19 and 61) and take the form

$$\tilde{g}_{ij}(r_{ij}) = \tilde{c}_{ij} e^{-\tilde{b}_{ij} r_{ij}} \sum_{k=0}^4 \frac{(\tilde{b}_{ij} r_{ij})^k}{k!}, \quad (20)$$

similar to the form used to model the short-ranged damping of the dispersion interactions. The charge-ordered nature of an ionic liquid means that the short-range terms are controlled entirely by the cation-anion interactions. Hence, $\tilde{c}_{\text{NaNa}} = \tilde{c}_{\text{ClCl}} = 0$.

A dipolar PIM requires two sets of parameters: the dipole polarizabilities, α_i , and the short-range damping parameters, \tilde{b}_{ij} and \tilde{c}_{ij} . The former characterize the response of an ion's electron density to the internal electric field that arises from the presence of both the formal ion charges and the induced dipole moments on the other ions. The latter control the effect of overlap of the nearest-neighbor electron density on the induced dipole moments.^{62–64} The dipole polarizabilities are obtained from *ab initio* electronic structure calculations in which ions are studied in the condensed phase.^{61,65} The short-range damping parameters are obtained from *ab initio* calculations by applying specific distortions to the nearest-neighbor shell of counter-ions.^{62–64} The remaining parameters controlling the short-range interactions are obtained by “force-fitting” methods (see Ref. 66 for full details). System properties, here the ion forces and cell stresses, are fitted to those extracted from the density-functional-based electronic structure calculations. Dispersion terms are parameterized from the ion polarizability.

The parameters describing $U_{\text{sr}}(r_{ij})$ are listed in Table I. In addition, the damping parameters for the dispersion interactions were fixed at $\tilde{b}_6^{ij} = \tilde{b}_8^{ij} = 1.7$ au; the polarizability of the Na^+ and Cl^- ions

TABLE I. Parameters used for the modified Born–Mayer potential [Eq. (18)]. The parameters correspond to atoms i and j of the chemical species α and β , respectively. All are listed in atomic units.

$\alpha\beta$	a_{ij}	B_{ij}	C_{ij}^6	C_{ij}^8
NaNa	5.0	1.0	10.0	100.0
ClCl	2.751	179.7	140.0	280.0
NaCl	1.726	67.5	37.4.0	167.3

was 0.89 and 20.0 au, respectively; and the short-range damping parameters [Eq. (20)] were $\tilde{b}_{\text{NaCl}} = \tilde{b}_{\text{ClNa}} = 1.76$ au, $\tilde{c}_{\text{ClNa}} = 3.0$ au, and $\tilde{c}_{\text{NaCl}} = 0.697$ au.

Simulations were also performed using two RIMs. In a RIM, there are no induction effects, so the Coulombic interaction energy reduces to $U_{\text{Coul}}(r_{ij}) = q_i T q_j$. In the first model, termed RIM1, the ion polarization terms were simply omitted, so the model retains the asymmetry of the short-range interactions between the Na–Na and Cl–Cl ion pairs resulting from differences in both their respective sizes and dispersion interactions. In the second model, termed RIM2, the like-ion short-ranged interactions were also set to zero and all dispersion interactions were removed, so the model maps onto an effective RPM, which shows symmetry in the interactions between the like ions that is broken in the more complete model. In the RPM, the ions are treated as hard-spheres, whereas in the RIM2, the repulsive wall is steep but finite-ranged. This difference of detail should not affect the cation–cation or anion–anion interactions because Coulomb ordering ensures the absence of like-ion nearest-neighbor contacts. There will be an effect, however, on the short-ranged cation–anion interactions, but this is not expected to alter substantially the long-ranged asymptotic behavior of the associated pair-correlation function.

V. MOLECULAR DYNAMICS SIMULATIONS

The PIM molecular dynamics simulation was performed in the NpT ensemble in order to assess the ability of the potential model to reproduce the equation of state for the liquid. The fluctuations in the pressure were around the atmospheric value. RIM simulations were performed in the NVT ensemble using the density obtained at each temperature from the NpT PIM simulations. The system contained 1728 NaCl molecules in a tetragonal cell with side lengths $L_x = 2L_y = 2L_z$. This cell geometry was chosen in order to maximize the accessible r -space distance range at an affordable computational cost. A constant temperature was maintained using a Nosé–Hoover thermostat,^{67,68} and a constant pressure was maintained using a barostat.⁶⁹ Crystalline configurations were melted at a temperature of $T = 5000$ K, well above the estimated melting point, and the temperature was then reduced to the required value and equilibrated for 50 000 time steps (≈ 30 ps). Production runs were of 1 700 000 time steps (≈ 1 ns) for the RIM and 600 000 time steps (≈ 360 ps) for the PIM. The PIM simulations are approximately one order of magnitude slower than their RIM counterparts because of the need to evaluate many-body interactions.

A. Large- r corrections

In the calculation of the large- r behavior of the pair-correlation functions, it is important to consider the finite size of the simulation cell. In the large- r limit,^{70,71}

$$g_{\alpha\beta}(r \rightarrow \infty) = 1 - \frac{S_{\alpha\beta}^{\text{FZ}}(0)}{\sqrt{N_{\alpha}N_{\beta}}}, \quad (21)$$

where N_{α} and N_{β} are the number of particles of chemical species α and β , respectively. Equation (21) provides the correction that must be applied to the calculated $g_{\alpha\beta}(r)$ function, where $S_{\alpha\beta}^{\text{FZ}}(0)$ is found from simulation by extrapolation at low- k .

The number-number partial pair-distribution function is given by

$$g_{\text{NN}}^{\text{BT}}(r) = c_{\text{M}}^2 g_{\text{MM}}(r) + c_{\text{X}}^2 g_{\text{XX}}(r) + 2c_{\text{M}}c_{\text{X}}g_{\text{MX}}(r). \quad (22)$$

In the case of an MX system for which $N_{\text{M}} = N_{\text{X}}$ and $c_{\text{M}} = c_{\text{X}} = 1/2$, the large- r limit is given by

$$g_{\text{NN}}^{\text{BT}}(r \rightarrow \infty) = 1 - \frac{1}{N_{\text{M}}} S_{\text{NN}}^{\text{BT}}(0). \quad (23)$$

Similarly, the large- r limit of the concentration-concentration partial pair-distribution function

$$g_{\text{CC}}^{\text{BT}}(r) = c_{\text{M}}c_{\text{X}}[g_{\text{MM}}(r) + g_{\text{XX}}(r) - 2g_{\text{MX}}(r)] \quad (24)$$

is given by

$$g_{\text{CC}}^{\text{BT}}(r \rightarrow \infty) = \frac{1}{N_{\text{M}}} \left[1 - \frac{S_{\text{CC}}^{\text{BT}}(0)}{c_{\text{M}}c_{\text{X}}} \right], \quad (25)$$

and the large- r limit of the number-concentration partial pair-distribution function

$$g_{\text{NC}}^{\text{BT}}(r) = c_{\text{M}}[g_{\text{MM}}(r) - g_{\text{MX}}(r)] - c_{\text{X}}[g_{\text{XX}}(r) - g_{\text{MX}}(r)] \quad (26)$$

is given by

$$g_{\text{NC}}^{\text{BT}}(r \rightarrow \infty) = -\frac{1}{N_{\text{M}}} \frac{S_{\text{NC}}^{\text{BT}}(0)}{c_{\text{M}}c_{\text{X}}}. \quad (27)$$

VI. RESULTS

A. Density

Figure 2 shows the temperature dependence of the number density obtained from experiment^{49,72–79} and the PIM simulations. The latter are in the range found by experiment and are larger than the values obtained from previous simulation work,⁸⁰ reflecting the effect of including the ion polarization.

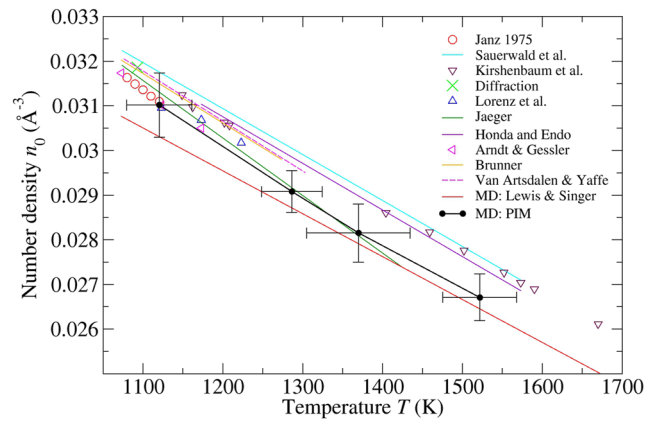


FIG. 2. Temperature dependence of the atomic number density of the melt from experiment^{49,72–79} and from molecular dynamics (MD) simulations: present work using the PIM (black circles with error bars) vs Lewis and Singer⁸⁰ (red curve). Also shown is the value used in the present diffraction work (green cross).

B. Total structure factors

Figure 3 shows the total structure factors $^{35}\text{F}(k)$ and $^{\text{nat}}\text{F}(k)$ and the difference function $\Delta F(k)$ measured by neutron diffraction. The x-ray total structure factor $S_{\text{X}}(k)$ is also shown and is compared to the function measured in the work of Ohno and Furukawa.^{30,81} Discrepancies can be attributed to the use, in the present work, of high-energy x rays to reduce the attenuation corrections and a diffractometer with a vacuum chamber to minimize the background scattering.

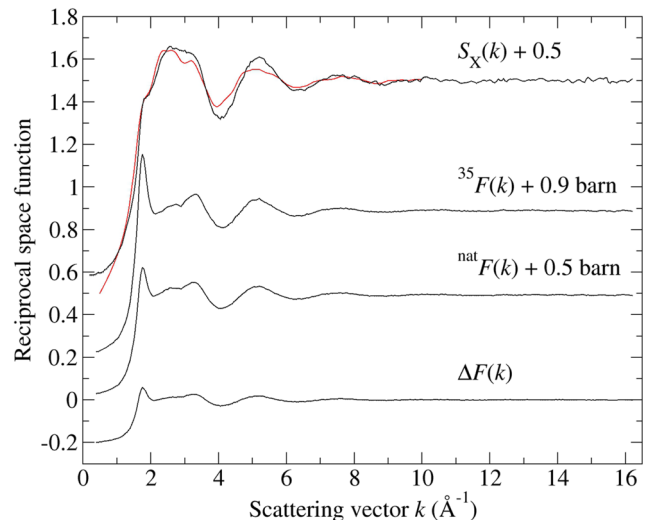


FIG. 3. The neutron total structure factors $^{35}\text{F}(k)$ and $^{\text{nat}}\text{F}(k)$ and the difference function $\Delta F(k)$ measured for NaCl at 1093 K compared to the x-ray total structure factor $S_{\text{X}}(k)$ measured for NaCl at 1091 K (black lines with vertical error bars). Also shown is the $S_{\text{X}}(k)$ function measured for NaCl at 1083 K in the work of Ohno and Furukawa^{30,81} (red curve).

C. Partial structure factors

Figure 4 compares the measured FZ partial structure factors with those obtained from the neutron diffraction work of Biggin and Enderby¹⁶ and the PIM simulation. The PIM results are in good agreement with the functions measured in the present work, reproducing the principal peak position at $k \approx 1.74 \text{ \AA}^{-1}$ and the form of the high- k oscillations.

Figure 5 compares the measured BT partial structure factors with those obtained from the PIM simulation. Also shown are the contributions to the simulated $S_{ij}^{\text{BT}}(k)$ functions from the weighted FZ partial structure factors. The insets highlight the low- k regions, plotted as a function of k^2 in order to fit a straight line and obtain both the gradient and $k \rightarrow 0$ limit.

For $S_{\text{NN}}^{\text{BT}}(k)$, the cancellation at $k \sim 1.74 \text{ \AA}^{-1}$ of the principal peaks in the NaNa and ClCl partial structure factors with the principal trough in the NaCl partial structure factor leads to a broad first peak at $k \sim 2.5 \text{ \AA}^{-1}$. The high- k oscillations are dominated by the fluctuations in $S_{\text{NaCl}}^{\text{FZ}}(k)$ [Fig. 5(a)]. In contrast, there is a sharp principal peak in $S_{\text{CC}}^{\text{BT}}(k)$ at $k \sim 1.74 \text{ \AA}^{-1}$ that has a significant contribution from all three of the FZ partial structure factors [Fig. 5(b)]. The high- k oscillations are again dominated by the contribution from $S_{\text{NaCl}}^{\text{FZ}}(k)$. For $S_{\text{NC}}^{\text{BT}}(k)$, there is no contribution from the NaCl partial structure factor and the similarity between the NaNa and ClCl partial structure factors leads to a weak principal peak at $k \sim 1.74 \text{ \AA}^{-1}$ and to a near-cancellation of the high- k oscillations [Fig. 5(c)].

The prominent principal peak in $S_{\text{CC}}^{\text{BT}}(k) = c_{\text{M}}c_{\text{X}}S_{\text{ZZ}}(k)$ corresponds to the Coulomb ordering of the ions.¹³ The lack of significant structure in $S_{\text{NN}}^{\text{BT}}(k)$ indicates only weak topological ordering, in stark contrast to molten glass-forming MX_2 systems, such as ZnCl_2 .^{55,82,83}

D. Partial pair-distribution functions

Figure 6 compares the measured partial pair-distribution functions $g_{\alpha\beta}(r)$ with those obtained from the neutron diffraction work

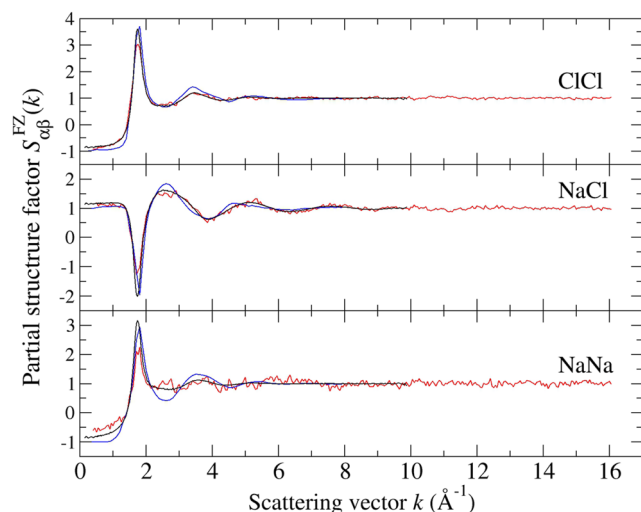


FIG. 4. Faber–Ziman partial structure factors from the present diffraction work at $T = 1093 \text{ K}$ (red curves), the neutron diffraction work of Biggin and Enderby at $T = 1148 \text{ K}$ ¹⁶ (blue curves), and the PIM simulation at $T = 1100 \text{ K}$ (black curves).

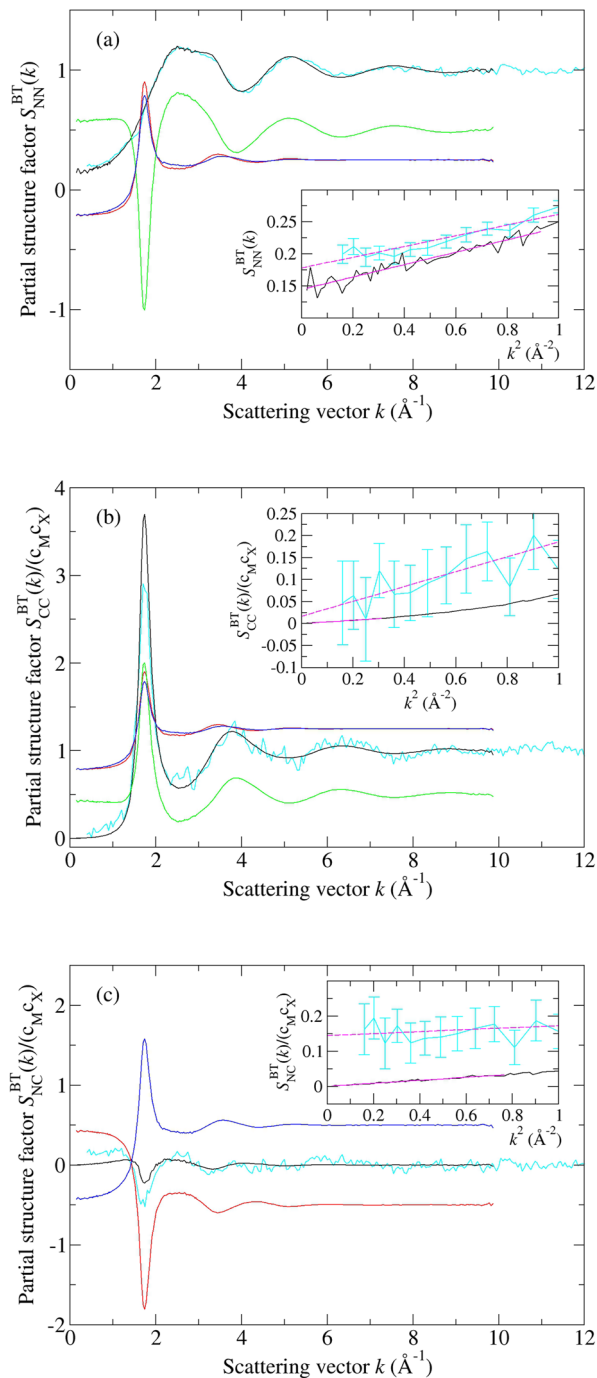


FIG. 5. Bhatia–Thornton partial structure factors (a) $S_{\text{NN}}^{\text{BT}}(k)$, (b) $S_{\text{CC}}^{\text{BT}}(k)/c_{\text{M}}c_{\text{X}}$, and (c) $S_{\text{NC}}^{\text{BT}}(k)/c_{\text{M}}c_{\text{X}}$ from experiment at $T = 1093 \text{ K}$ (present work, cyan curves) and the PIM simulation at $T = 1100 \text{ K}$ (black curves). Also shown is the breakdown of the simulated functions into their contributions from the weighted FZ partial structure factors $S_{\text{ClCl}}^{\text{FZ}}(k)$ (red curves), $S_{\text{NaCl}}^{\text{FZ}}(k)$ (green curves), and $S_{\text{NaNa}}^{\text{FZ}}(k)$ (blue curves). The insets highlight the measured and simulated BT functions at low- k , plotted as a function of k^2 in order to extract the low-order moments by fitting a straight line. The fitted functions are shown by the broken magenta and solid magenta lines, respectively.

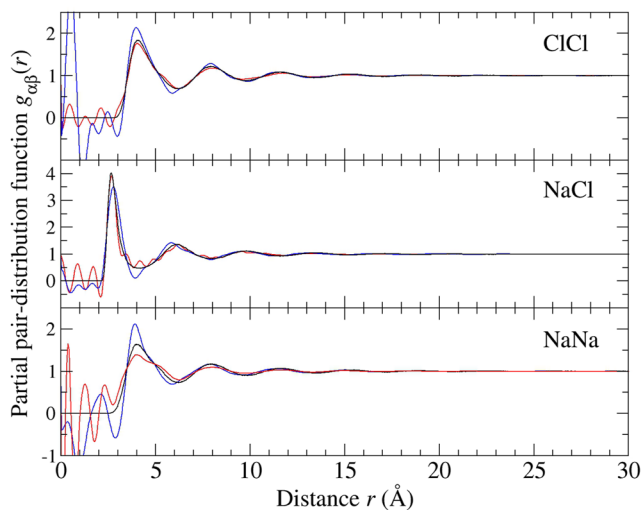


FIG. 6. Partial pair-distribution functions from the present diffraction work at $T = 1093$ K (red curves), the neutron diffraction work of Biggin and Enderby¹⁶ at $T = 1148$ K (blue curves), and the PIM simulation at $T = 1100$ K (black curves).

of Biggin and Enderby¹⁶ and the PIM simulation. The measured functions were obtained by Fourier transforming the partial structure factors, which accounts for the low- r oscillations about zero at distances smaller than the distance of closest approach between two ions. In the present diffraction work, these features do not have a significant contribution from the truncation effects associated with terminating $S_{\alpha\beta}^{\text{FZ}}(k)$ at the maximum accessible value $k_{\text{max}} \approx 16 \text{ \AA}^{-1}$ because the measured functions do not show oscillations that extend beyond k_{max} . Low- r oscillations are absent from the simulated $g_{\alpha\beta}(r)$ functions because they are generated from direct knowledge of the ion positions. The nearest-neighbor distances and coordination numbers are summarized in Table II. The simulated functions are in excellent agreement with those obtained from the present diffraction work in terms of the first peak position, coordination number, and longer-range oscillations although the first peak in $g_{\text{NaNa}}(r)$ is more intense.

Figure 7 compares the measured BT partial pair-distribution functions with those obtained from the PIM simulation. Also shown are the contributions to $g_{IJ}^{\text{BT}}(r)$ from the weighted $g_{\alpha\beta}(r)$ functions obtained from the simulation. For $g_{\text{NN}}^{\text{BT}}(r)$, the first peak at $r \approx 2.68 \text{ \AA}$

has a strong contribution from $g_{\text{NaCl}}(r)$ and therefore originates from the packing of ions with unlike charges. The oscillations that extend to larger distances have a periodicity of the order half that of the underlying $g_{\alpha\beta}(r)$ functions. For $g_{\text{CC}}^{\text{BT}}(r)$, there is a sharp principal trough at $r \approx 2.68 \text{ \AA}$ followed by oscillations that extend to large r -values, which reflects the Coulomb ordering. In contrast, $g_{\text{NC}}^{\text{BT}}(r)$ is almost featureless, reflecting the similarity between $g_{\text{NaNa}}(r)$ and $g_{\text{ClCl}}(r)$ and the weak coupling between the charge and number density fluctuations.¹³

VII. DISCUSSION

A. Thermodynamics

The Fourier transform relations between the BT partial structure factors and corresponding partial pair-distribution functions can be written as

$$S_{\text{NN}}^{\text{BT}}(k) - 1 = \frac{4\pi n_0}{k} \int_0^\infty dr [g_{\text{NN}}(r) - 1] r \sin(kr), \quad (28)$$

$$\frac{S_{\text{CC}}^{\text{BT}}(k)}{c_{\text{M}} c_{\text{X}}} - 1 = \frac{4\pi n_0}{k} \int_0^\infty dr g_{\text{CC}}(r) r \sin(kr), \quad (29)$$

$$\frac{S_{\text{NC}}^{\text{BT}}(k)}{c_{\text{M}} c_{\text{X}}} = \frac{4\pi n_0}{k} \int_0^\infty dr g_{\text{NC}}(r) r \sin(kr). \quad (30)$$

The low- k behavior of the BT partial structure factors can be found by making a Taylor expansion of $\sin(kr)$ such that⁸⁵

$$S_{\text{NN}}^{\text{BT}}(k) - 1 = M_{\text{NN}}^{(0)} + M_{\text{NN}}^{(2)} k^2 + M_{\text{NN}}^{(4)} k^4 + \dots, \quad (31)$$

$$\frac{S_{\text{CC}}^{\text{BT}}(k)}{c_{\text{M}} c_{\text{X}}} - 1 = M_{\text{CC}}^{(0)} + M_{\text{CC}}^{(2)} k^2 + M_{\text{CC}}^{(4)} k^4 + \dots, \quad (32)$$

$$\frac{S_{\text{NC}}^{\text{BT}}(k)}{c_{\text{M}} c_{\text{X}}} = M_{\text{NC}}^{(0)} + M_{\text{NC}}^{(2)} k^2 + M_{\text{NC}}^{(4)} k^4 + \dots. \quad (33)$$

The moments $M_{IJ}^{(2m)}$, where $m = 0, 1, 2, \dots$, are obtained from the $r_{\text{max}} \rightarrow \infty$ limit of the running moments defined by

$$\text{run } M_{IJ}^{(2m)}(r_{\text{max}}) = \int_0^{r_{\text{max}}} dr \rho_{IJ}^{(2m)}(r). \quad (34)$$

TABLE II. The nearest-neighbor distances $\bar{r}_{\alpha\beta}$ and coordination numbers \bar{n}_{α}^{β} for molten NaCl. The datasets were taken from experiments using neutron diffraction with isotope substitution (NDIS), with and without high-energy x-ray diffraction (XRD), and from the PIM molecular dynamics (MD) simulation. The distances were taken from the first peak position in $g_{\alpha\beta}(r)$, and the coordination numbers were obtained by integrating over the first peak in $g_{\alpha\beta}(r)$ to the first minimum.

Method	T (K)	\bar{r}_{NaCl} (Å)	$\bar{n}_{\text{Na}}^{\text{Cl}}$	\bar{r}_{NaNa} (Å)	$\bar{n}_{\text{Na}}^{\text{Na}}$	\bar{r}_{ClCl} (Å)	$\bar{n}_{\text{Cl}}^{\text{Cl}}$	Reference
NDIS + XRD	1093	2.68 (1)	4.7 (1)	4.01 (2)	15.2 (5)	4.03 (2)	15.1 (5)	This work
NDIS	1148	2.78 (2)	5.3 (4)	3.96 (3)	...	3.91 (3)	...	16
PIM MD	1100	2.66 (1)	5.2 (1)	4.05 (2)	15.4 (5)	4.07 (2)	15.3 (5)	This work

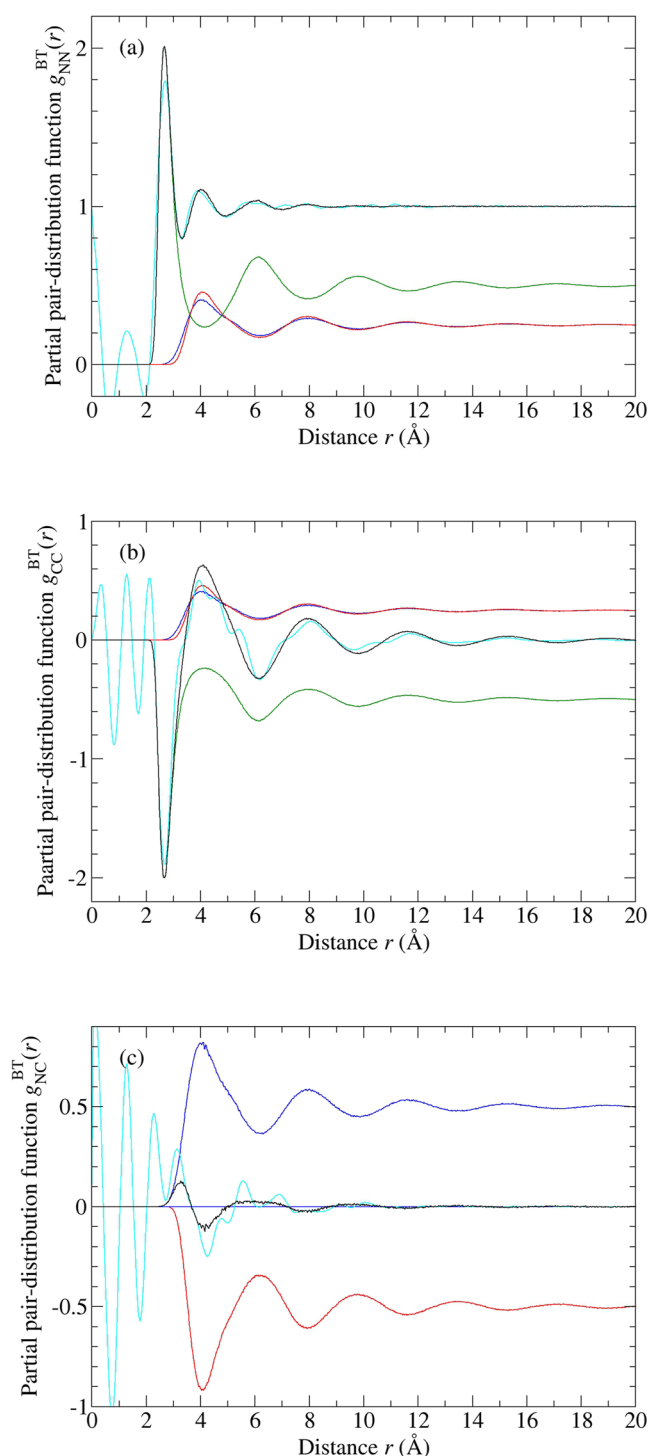


FIG. 7. Bhatia–Thornton partial pair-distribution functions (a) $g_{NN}^{BT}(r)$, (b) $g_{CC}^{BT}(r)$, and (c) $g_{NC}^{BT}(r)$ from the present diffraction work (cyan curves) and from the PIM simulation (black curves). Also shown is the breakdown of the simulated functions into their contributions from the weighted $g_{ClCl}(r)$ (red curves), $g_{NaCl}(r)$ (green curves), and $g_{NaNa}(r)$ (blue curves) functions.

In the case of the number density fluctuations,

$$\rho_{NN}^{(2m)}(r) = \frac{4\pi n_0 (-1)^m}{(2m+1)!} [g_{NN}^{BT}(r) - 1] r^{2m+2}. \quad (35)$$

Equivalent expressions define the $\rho_{ij}^{(2m)}(r)$ functions corresponding to $g_{CC}^{BT}(r)$ and $g_{NC}^{BT}(r)$. Figure 8 shows the running moments for $m = 0$ obtained from the PIM simulations at $T = 1100$ K.

As discussed in Sec. II, $S_{CC}^{BT}(0) = S_{NC}^{BT}(0) = 0$ for an ionic system. It follows that in the limit as $r_{\max} \rightarrow \infty$, the $m = 0$ moments are given by

$$M_{NN}^{(0)} = S_{NN}^{BT}(0) - 1 = n_0 k_B T \chi_T - 1, \quad (36)$$

$$M_{CC}^{(0)} = \frac{S_{CC}^{BT}(0)}{c_M c_X} - 1 = -1, \quad (37)$$

$$M_{NC}^{(0)} = \frac{S_{NC}^{BT}(0)}{c_M c_X} = 0. \quad (38)$$

These moments deliver therefore the $k \rightarrow 0$ limiting behavior of the BT partial structure factors. The other moments deliver the low- k behavior. For example, in the case of the concentration fluctuations,

$$M_{CC}^{(2)} \equiv \text{run } M_{CC}^{(2)}(r_{\max} \rightarrow \infty) = \Lambda_D^2 \quad (39)$$

such that in the low- k region,

$$S_{CC}^{BT}(k)/c_M c_X = \Lambda_D^2 k^2. \quad (40)$$

Figure 9 compares the χ_T value found from the diffraction results by fitting a straight line to $S_{NN}^{BT}(k)$ vs k^2 in the low- k region and extrapolating to the $k \rightarrow 0$ limit [Eq. (31)] with the values found

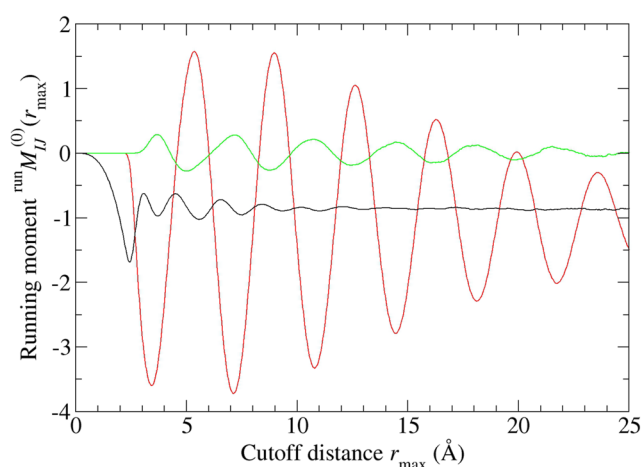


FIG. 8. Running moments $\text{run } M_J^{(0)}(r_{\max})$ from the PIM simulations at $T = 1100$ K for $J = NN$ (black curve), CC (red curve), and NC (green curve).

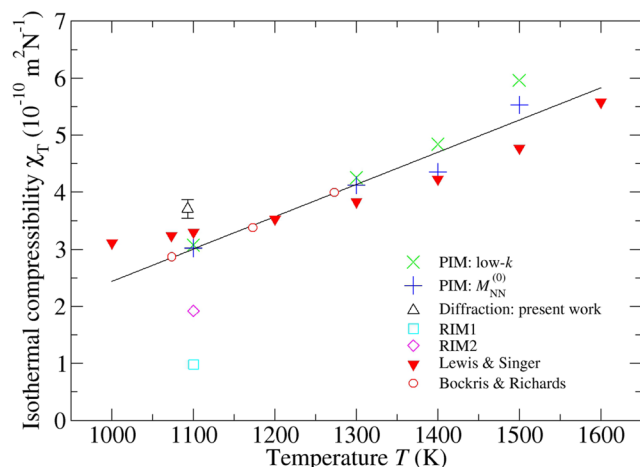


FIG. 9. Temperature dependence of the isothermal compressibility. The values obtained from the sound velocity measurements of Bockris and Richards,⁸⁴ fitted to a straight (black) line, are compared to the value found from the low- k behavior of $S_{NN}^{BT}(k)$ in the present diffraction work and to the values obtained from the PIM simulation via both the low- k behavior of $S_{NN}^{BT}(k)$ and the moment $M_{NN}^{(0)}$ [Eq. (36)]. Also shown are the values obtained from the RIM1 and RIM2 simulations obtained from the low- k behavior of $S_{NN}^{BT}(k)$.

from sound velocity experiments.⁸⁴ Figure 9 also shows the results obtained from the PIM simulations, where χ_T was found from either (i) the low- k behavior of $S_{NN}^{BT}(k)$ in the same way as for the diffraction work or (ii) by calculating $M_{NN}^{(0)}$ from the data shown in Fig. 8 [see Eq. (36)]. The difference in the values calculated from $S_{NN}^{BT}(k)$ and $M_{NN}^{(0)}$ reflects the errors associated with obtaining both the low- k and high- r limits, respectively. The simulated results show good agreement with experiment over the measured range of temperatures up to ~ 1273 K. The deviation of the PIM compressibility from the linearly extrapolated experimental values at high temperatures may therefore reflect genuine behavior.

Table III lists the values of Λ_D^2 extracted from the molecular dynamics results by fitting a straight line to $S_{CC}^{BT}(k)/c_{MCX}$ vs k^2 in the low- k region [Eq. (40)]. The fitted functions are shown in the insets to Figs. 5(b) and 11(b). In comparison, it is often assumed that ϵ_r can be set to the high-frequency dielectric constant ϵ_∞ obtained from the refractive index n measured at optical wavelengths via the relationship $\epsilon_\infty = n^2$. For molten NaCl at 1093 K, the measured value is between $n = 1.413$ (Na lamp, wavelength 5893 Å) and $n = 1.424$ (Hg lamp, wavelength 5461 Å).⁴⁵ It follows from Eq. (10)

TABLE III. The Debye screening lengths obtained from the low- k behavior of $S_{CC}^{BT}(k)$, the number density, and the relative permittivity obtained from Eq. (10) for the PIM vs RIM1 and RIM2 simulations at $T = 1100$ K.

	Λ_D^2 (Å ²)	n_0 (Å ⁻³)	ϵ_r
PIM	0.035 92	0.031 46	2.157
RIM1/RIM2	0.021 69	0.031 46	1.302

that $\Lambda_D^2 = 0.0326\text{--}0.0331$ Å², close to the value obtained from the PIM simulation. In the case of the diffraction work, a straight line fit to $S_{CC}^{BT}(k)/c_{MCX}$ vs k^2 in the low- k region [see the inset to Fig. 5(b)] gives $S_{CC}^{BT}(0)/c_{MCX} = 0.016(16)$ or $S_{CC}^{BT}(0) = 0.004(4)$ with $\Lambda_D^2 = 0.17(2)$ Å². The latter is therefore larger than expected, which reflects the experimental error.

In the case of $S_{NC}^{BT}(k)$, the $k \rightarrow 0$ limit found from the diffraction work by fitting a straight line to $S_{NC}^{BT}(k)/c_{MCX}$ vs k^2 in the low- k region was 0.144(12) [see the inset to Fig. 5(c)]. Hence, $S_{NC}^{BT}(0) = 0.036(3)$ instead of the theoretically expected value of zero. This discrepancy reflects the small magnitude of the NC partial structure factor and its sensitivity to the experimental error (Sec. III C).

B. Comparison with the RIMs

Figure 10 compares the FZ partial structure factors from the PIM simulations with those obtained from the rigid-ion models described in Sec. IV. As expected, the $S_{NaNa}^{FZ}(k)$ and $S_{ClCl}^{FZ}(k)$ functions are identical for the RIM2, which is equivalent to an effective RPM. The effect of including ion polarization (RIM1 \rightarrow PIM) is to reduce the height of the principal peak or trough at $k \sim 1.74$ Å⁻¹, corresponding to a reduction in the magnitude of the oscillations in the partial pair-distribution functions. This effect is most pronounced for $S_{NaNa}^{FZ}(k)$ and corresponds to an increase in the mobility of the Na⁺ cations. At $T = 1200$ K, for example, the self-diffusion coefficients for the Na⁺ and Cl⁻ ions are $D_{Na} = 8.8 \times 10^{-5}$ cm² s⁻¹ and $D_{Cl} = 7.2 \times 10^{-5}$ cm² s⁻¹, respectively, for the PIM as compared to $D_{Na} = 6.2 \times 10^{-5}$ cm² s⁻¹ and $D_{Cl} = 5.6 \times 10^{-5}$ cm² s⁻¹, respectively, for the RIM1. The inclusion of polarization terms tends to lower the activation barrier associated with the motion of an ion by facilitating charge screening during each step in a diffusion pathway, e.g., as an ion “squeezes” through the nearest-neighbor coordination shell of its counter-ions.¹²

Figure 11 shows the BT partial structure factors obtained from the different models at 1100 K and compares them to the functions

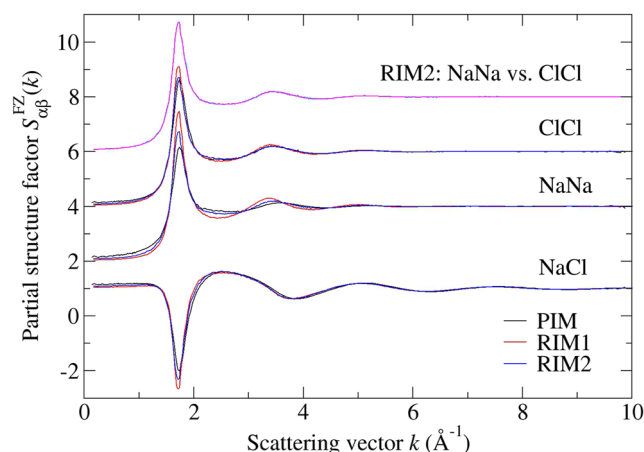


FIG. 10. FZ partial structure factors calculated for molten NaCl at $T = 1100$ K using the PIM, RIM1, and RIM2. The ClCl and NaNa functions are shifted along the ordinate axis for clarity of presentation. RIM2 is equivalent to an effective RPM, and as expected, the NaNa and ClCl partial structure factors for this model are identical within the statistical error.

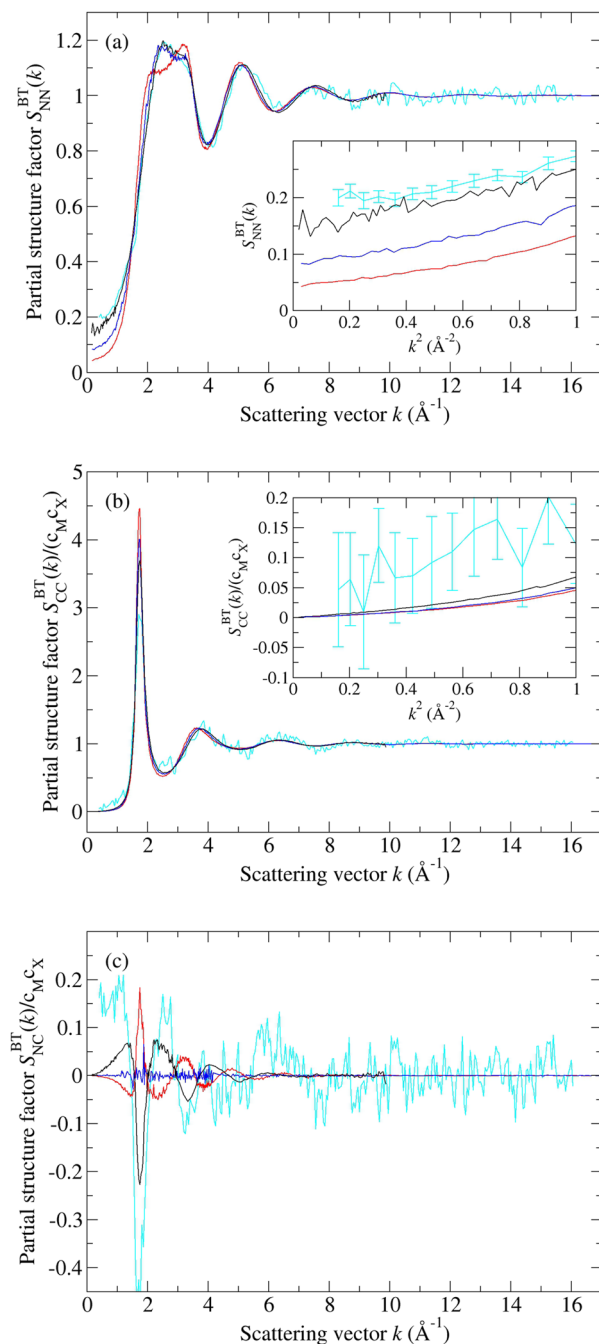


FIG. 11. Bhatia–Thornton partial structure factors calculated for molten NaCl at $T = 1100$ K using the PIM (black curves), RIM1 (red curves), and RIM2 (blue curves). The cyan curves show the functions measured in the present diffraction work. The insets in (a) and (b) zoom into the low- k region of the simulated and measured functions.

obtained from the diffraction work. For $S_{NN}^{BT}(k)$, the PIM results show the best agreement with experiment in terms of the main peak structure in the k -range of ~ 2 – 3.5 \AA^{-1} , the oscillations at high- k , and the low- k behavior as highlighted in the inset to Fig. 11(a). Both

RIMs give smaller low- k limits than either the PIM or experiment, corresponding to systems that are less compressible. The isothermal compressibility values predicted by the PIM, RIM1, and RIM2 are shown in Fig. 9. For $S_{CC}^{BT}(k)$, the principal peak is more intense for both of the RIMs, which accompanies a more intense principal peak or trough in the associated $S_{\alpha\beta}^{FZ}(k)$ functions. For $S_{NC}^{BT}(k)$, the near-cancellation of the contributions from the underlying FZ functions leads to more dramatic differences between the different models. For the RIM2, the symmetric nature of the like-ion interactions leads to near perfect cancellation, so $S_{NC}^{BT}(k) \approx 0$. For the RIM1, the balance of the principal peak intensities in the underlying FZ functions results in a principal peak that is inverted with respect to that extracted from experiment or the PIM.

C. Decay of the pair-correlations

According to simple theory for the RPM in which the ion interactions are described by pairwise additive potentials having short-ranged repulsive and Coulomb terms with no induction of dispersion effects, the asymptotic behavior of the total pair-correlation functions $rh_{\alpha\beta}(r)$ is given by

$$rh_{\alpha\beta}(r) \rightarrow 2|A_{\alpha\beta}| \exp(-a_0^{\alpha\beta} r) \cos(a_1^{\alpha\beta} r - \theta_{\alpha\beta}). \quad (41)$$

In Eq. (41), $h_{\alpha\beta}(r) = g_{\alpha\beta}(r) - 1$, all three $rh_{\alpha\beta}(r)$ functions share a common decay length $[a_0^{\alpha\beta}]^{-1}$ and a common wavelength of oscillation $2\pi/a_1^{\alpha\beta}$, the amplitudes are related by $|A_{MM}||A_{XX}| = |A_{MX}|^2$, and the phases are related by $\theta_{MM} + \theta_{XX} = 2\theta_{MX}$.²⁴ Similarly, the asymptotic behavior of the BT total pair-correlation functions $rh_{NN}^{BT}(r) = r[S_{NN}^{BT}(r) - 1]$, $rh_{CC}^{BT}(r) = r g_{CC}^{BT}(r)$, and $rh_{NC}^{BT}(r) = r g_{NC}^{BT}(r)$ can be written as³⁶

$$rh_{IJ}^{BT}(r) \rightarrow 2|A_{IJ}| \exp(-a_0^{IJ} r) \cos(a_1^{IJ} r - \theta_{IJ}). \quad (42)$$

In the RPM, the M^+ and X^- ions have the same size, and $g_{MM}(r) = g_{XX}(r)$ such that $g_{NC}^{BT}(r) = 0$, i.e., the concentration (or charge) and number density fluctuations are decoupled. In this case, there is no requirement for $rh_{NN}^{BT}(r)$ and $rh_{CC}^{BT}(r)$ to share the same asymptotic behavior.³⁶ If $rh_{CC}^{BT}(r)$ decays more slowly than $rh_{NN}^{BT}(r)$, it is expected that the amplitudes of $rh_{MM}(r) = rh_{XX}(r)$ and rh_{MX} will be equal but opposite in sign and that $\theta_{MM} = \theta_{XX} = \theta_{MX}$, i.e., $rh_{MM}(r) = rh_{XX}(r) = -rh_{MX}(r)$ at the longest range.²⁴ For molten NaCl, $g_{NC}^{BT}(r) \neq 0$, but it has, nevertheless, a small magnitude. The large- r behavior of the total pair-correlation functions should therefore resemble that of the RPM.

Figure 12 shows the $rh_{\alpha\beta}(r)$ functions obtained from the RIM2 simulations along with the large- r fits to these functions using Eq. (41). The fitted parameters are summarized in Table IV. The results show that $rh_{MM}(r) \approx rh_{XX}(r) \approx -rh_{MX}(r)$ at the longest range as expected for the RPM. According to simple theory, the expected amplitude $|A_{MX}| = \pm\sqrt{|A_{MM}||A_{XX}|} = \pm 2.601(11)$ \AA , and the fitted value is 5% smaller than the positive root. The expected phase $\theta_{MX} = (\theta_{MM} + \theta_{XX})/2 = 1.353$ rad, but the fitted value is 4.405 rad. However, $|A| \cos(a_1 r - \theta) = -|A| \cos(a_1 r - \theta \pm \pi)$, so a phase shift of π , which is equivalent to taking the negative value for $|A_{MX}|$, gives 1.263 rad, i.e., a 7% smaller value. The longest decay length

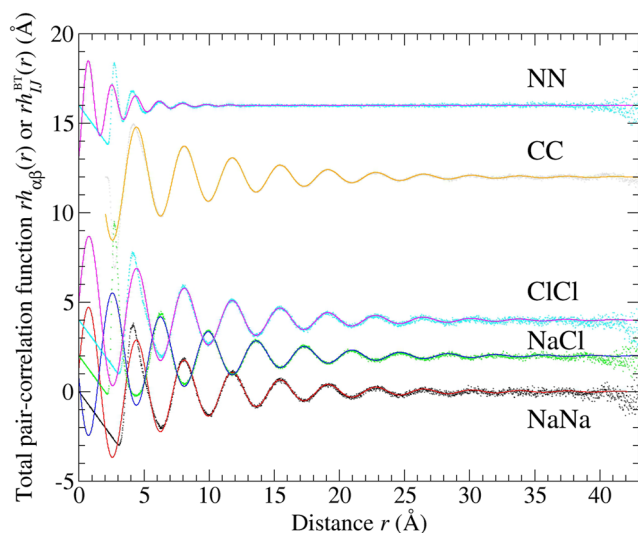


FIG. 12. The total pair-correlation functions obtained from the RIM2 simulations at $T = 1100$ K. At large- r values, the ion-ion functions $rh_{\alpha\beta}(r)$ ($\alpha\beta = \text{NaNa}$, ClCl or NaCl) are fitted to Eq. (41) and the BT functions $rh_{IJ}^{BT}(r)$ ($IJ = \text{NN}$ or CC) are fitted to Eq. (42). The datasets are shown by the points, and the fitted functions are shown by the solid curves.

$a_0^{-1} \sim 7.7$ Å is a factor of ≈ 2.9 times greater than the nearest-neighbor Na–Cl distance of 2.62 Å.

Figure 12 also shows the $rh_{IJ}^{BT}(r)$ functions obtained from the RIM2 simulations along with the large- r fits to these functions using Eq. (42). The fitted parameters are summarized in Table IV. The a_0^{BT} value for the NN correlations is ~ 3.3 times larger than the value for the CC correlations such that $rh_{NN}^{BT}(r)$ decays more quickly than $rh_{CC}^{BT}(r)$. Also, the a_1^{BT} value for the NN correlations is ~ 2 times larger than the value for the CC correlations such that the periodicity $2\pi/a_1^{BT}$ of the large- r oscillations in $rh_{NN}^{BT}(r)$ is roughly half that of the periodicity in $rh_{CC}^{BT}(r)$. This difference in the periodicity is also seen in the measured data sets and depends on the form of the underlying ion–ion partial pair-distribution functions. In the case of $rh_{CC}^{BT}(r)$, all three of these functions contribute [Fig. 7(b)] and their periodicity $2\pi/a_1^{\alpha\beta}$ is retained. In comparison, the large- r oscillations in $rh_{NN}^{BT}(r)$ have nearly half the wavelength of the

TABLE IV. Parameters obtained by fitting the total pair-correlation functions from the RIM2 simulations at $T = 1100$ K using either Eq. (41) with Na and Cl as the variables or Eq. (42) with N and C as the variables. r_1 and r_2 specify the fitted r -space range.

Pair	$ A $ (Å)	a_0 (Å ⁻¹)	a_1 (Å ⁻¹)	θ (rad)	r_1 (Å)	r_2 (Å)
NaNa	2.606(17)	0.134(6)	1.708(7)	1.326(6)	5.3	16.0
ClCl	2.596(13)	0.132(6)	1.713(6)	1.379(2)	5.3	16.0
NaCl	2.460(13)	0.130(5)	1.708(6)	4.405(9)	5.3	16.9
NN	1.700(3)	0.426(4)	3.463(8)	2.588(4)	3.0	8.0
CC	2.478(12)	0.130(4)	1.709(2)	1.335(7)	5.3	16.0

underlying ion–ion functions, reflecting a competition between the like and unlike ion–ion functions [Fig. 7(a)].

Figure 13 shows the BT total pair-correlation functions $rh_{IJ}^{BT}(r)$ obtained from the PIM simulations at four different temperatures

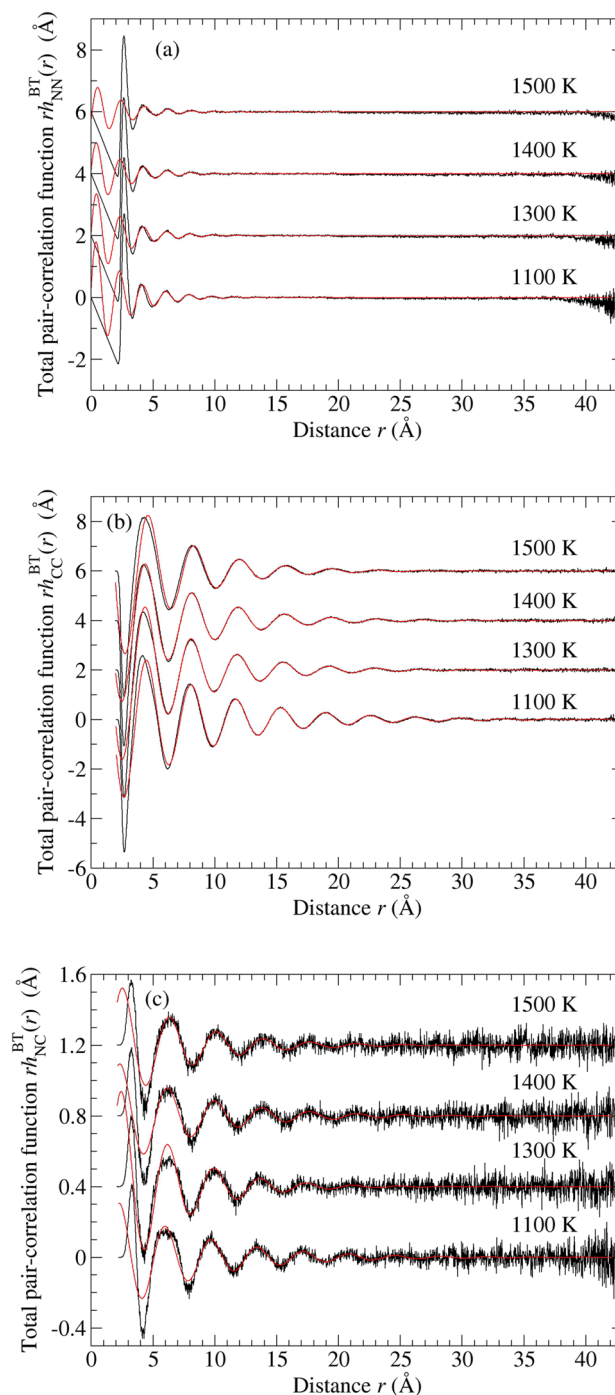


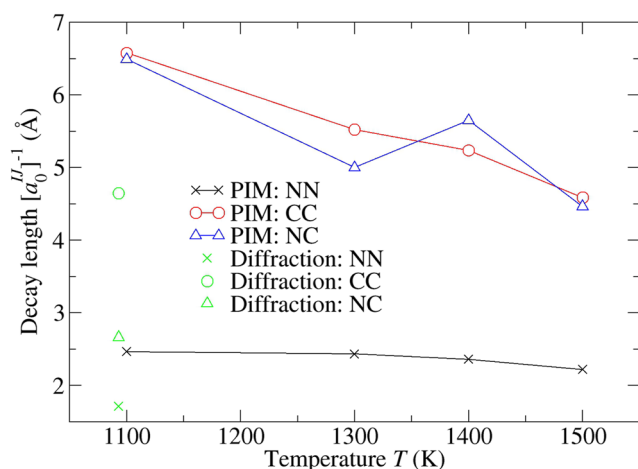
FIG. 13. Temperature dependence of the BT total pair-correlation functions (a) $rh_{NN}^{BT}(r)$, (b) $rh_{CC}^{BT}(r)$, and (c) $rh_{NC}^{BT}(r)$ from the PIM simulations (black curves) fitted to Eq. (42) (red curves).

TABLE V. Parameters obtained by fitting the total pair-correlation functions from experiment or the PIM simulations using either Eq. (41) with Na and Cl as the variables or Eq. (42) with N and C as the variables. r_1 and r_2 specify the fitted r -space range.

Pair	T (K)	$ A $ (Å)	a_0 (Å ⁻¹)	a_1 (Å ⁻¹)	θ (rad)	r_1 (Å)	r_2 (Å)
NaNa	1093 ^a	2.57(7)	0.237(3)	1.737(3)	1.51(2)	6.69	12.2
	1100	2.272(5)	0.154(7)	1.721(9)	1.320(8)	10	30
ClCl	1093 ^a	4.2(1)	0.231(4)	1.731(4)	1.42(4)	6.26	19.0
	1100	2.700(5)	0.152(8)	1.720(1)	1.280(6)	10	30
NaCl	1093 ^a	3.6(3)	0.24(1)	1.733(9)	4.65(7)	4.91	19.0
	1100	2.322(5)	0.149(9)	1.719(4)	4.420(5)	10	30
NN	1093 ^a	2.1(4)	0.59(5)	3.47(4)	1.2(2)	3.31	9.51
	1100	1.10(5)	0.406(1)	3.338(3)	1.370(6)	5	20
	1300	0.79(9)	0.411(7)	3.307(1)	1.460(6)	5	20
	1400	0.70(3)	0.424(9)	3.307(3)	1.594(1)	5	20
	1500	0.70(9)	0.451(2)	3.334(3)	1.948(4)	5	20
CC	1093 ^a	2.9(3)	0.22(1)	1.703(9)	1.16(8)	6.81	16.4
	1100	2.43(1)	0.152(3)	1.720(9)	1.294(1)	10	30
	1300	2.64(3)	0.181(3)	1.693(6)	1.278(3)	10	30
	1400	2.64(2)	0.191(1)	1.675(8)	1.159(5)	10	30
	1500	3.16(2)	0.218(6)	1.663(6)	1.154(4)	10	30
NC	1093 ^a	1.8(5)	0.38(5)	1.60(4)	3.6(2)	4.54	15.3
	1100	0.25(6)	0.154(9)	1.707(9)	4.123(2)	10	30
	1300	0.36(6)	0.200(1)	1.710(8)	4.510(8)	10	30
	1400	0.24(9)	0.177(2)	1.670(7)	4.214(4)	10	30
	1500	0.39(5)	0.224(9)	1.689(6)	4.660(2)	10	30

^aExperiment.

along with the fits to the large- r region of these functions using Eq. (42). The NC functions are relatively noisy, reflecting the near-cancellation of the underlying ion-ion partial pair-distribution functions [Fig. 7(c)]. The fitted parameters are listed in Table V, where

**FIG. 14.** Temperature dependence of the decay length $[a_0^{\text{II}}]^{-1}$ of Eq. (42). The values from the PIM simulations at several different temperatures are compared to the values from the diffraction experiment at $T = 1093$ K.

the a_0^{II} values are more sensitive to the fitted r -range than the a_1^{II} values. The results show that the large- r oscillations become increasingly damped with increasing temperature as the decay length decreases (Fig. 14). At sufficiently high temperatures, a crossover from exponentially damped oscillatory decay to pure exponential decay is expected.²⁵ Table V also lists the parameters obtained from fits to the large- r region of the associated ion-ion pair-distribution functions $rh_{\alpha\beta}(r)$ at $T = 1100$ K, where the fitted function is given by Eq. (41), along with the parameters obtained from the fitted diffraction data. The decay lengths a_0^{-1} extracted from experiment will represent lower bounds because the finite k -space resolution function of a diffractometer will lead to damped oscillations in the measured $rh(r)$ functions.³⁶

It is notable that when dispersion forces are present, the asymptotic decay of the $rh_{\text{II}}^{\text{BT}}(r)$ functions is expected to be governed by a power-law decay.³⁶ These forces are, however, expected to be weak, and their effect could not be readily identified when they were removed by switching from the PIM to the RIM2.

VIII. HEAT CAPACITY

The heat capacity was calculated from the gradient of the internal energy (which is equivalent to the enthalpy at zero pressure) as a function of temperature. The mean value obtained for the temperature interval 1100–1400 K is $c_p = 58.8 \text{ J K}^{-1} \text{ mol}^{-1}$ for the RIM1 vs $c_p = 69.9 \text{ J K}^{-1} \text{ mol}^{-1}$ for the PIM. These values compare to an

experimental heat capacity of $c_p \sim 67.8 \text{ J K}^{-1} \text{ mol}^{-1}$ at a temperature of 1250 K.⁸⁶ The value for the PIM is larger than for the RIM1 because the model has a greater number of degrees of freedom.

IX. CONCLUSIONS

The full set of partial pair-correlation functions for molten NaCl just above the melting point was measured by combining neutron diffraction with isotope substitution and high-energy x-ray diffraction. The experimental work was complemented by molecular dynamics simulations using a PIM and two RIMs. These models enable an exploration of the effect on the pair-correlation functions of removing the ion dispersion and polarization terms, thus allowing for an effective RPM to be accessed in which the anion and cation have equal but opposite charges and are otherwise identical.

The results for the effective RPM are in qualitative agreement with simple theory although there are discrepancies at large r -values in the amplitude and phase of the modeled and simulated total pair-correlation functions that may originate from the details of the fitting procedure. The PIM simulations give a good account of the measured density, partial pair-distribution functions, isothermal compressibility, and heat capacity. The Debye screening length is consistent with the approximation that $\epsilon_r = \epsilon_\infty = n^2$. The longest decay length from experiment or the PIM simulations $a_0^{-1} \approx 6.7 \text{ \AA}$ is a factor of ≈ 2.5 times greater than the nearest-neighbor Na–Cl distance of 2.7 \AA . The results are commensurate with those expected from the RPM, which predicts decay lengths much shorter than those found in experiments on concentrated electrolytes or ionic liquids using surface force apparatus.²⁹ The discrepancy in the asymptotic behavior of the pair-correlation functions between theory and surface force experiments does not therefore appear to originate from the approximations made in the RPM,²⁴ e.g., the equivalence in size of the counter-ions, the immersion of these ions in a uniform continuum with mean dielectric constant ϵ , and the omission of the ion polarizability.

ACKNOWLEDGMENTS

We thank Bob Evans (Bristol) for his encouragement of this work, Pierre Palleau (Grenoble) for his help with the neutron diffraction experiment, and Phil Jones (Bath) for his glass blowing expertise. The Bath group acknowledges the EPSRC for support via Grant No. EP/G008795/1. T.U. would like to thank the Japan Society for the Promotion of Science (JSPS) for financial support (Grant Nos. 20H02430 and 16H03903) and the Scientist Exchange Program between the JSPS and Royal Society.

AUTHOR DECLARATIONS

Conflict of Interest

The authors have no conflicts to disclose.

Author Contributions

Anita Zeidler: Data curation (equal); Formal analysis (equal); Investigation (equal); Methodology (equal); Software (equal); writing – review & editing (equal). **Philip S. Salmon:** Conceptualization (equal); Data curation (equal); Formal analysis (equal); Funding

acquisition (equal); Investigation (equal); Methodology (equal); writing – original draft (equal). **Takeshi Usuki:** Formal analysis (equal); Investigation (equal). **Shinji Kohara:** Formal analysis (equal); Investigation (equal). **Henry E. Fischer:** Investigation (equal). **Mark Wilson:** Conceptualization (equal); Data curation (equal); Formal analysis (equal); Investigation (equal); Methodology (equal); Software (equal); writing – original draft (equal).

DATA AVAILABILITY

The datasets created during this research are openly available from the University of Bath Research Data Archive at <https://doi.org/10.15125/BATH-01165>.⁸⁷

REFERENCES

- 1 M. M. Kenisarin, *Renewable Sustainable Energy Rev.* **14**, 955 (2010).
- 2 J. C. Gomez-Vidal and R. Tirawat, *Sol. Energy Mater. Sol. Cells* **157**, 234 (2016).
- 3 Z. Rong, J. Ding, W. Wang, G. Pan, and S. Liu, *Sol. Energy Mater. Sol. Cells* **216**, 110696 (2020).
- 4 W. Ding and T. Bauer, *Engineering* **7**, 334 (2021).
- 5 H. Kim, D. A. Boysen, J. M. Newhouse, B. L. Spatocco, B. Chung, P. J. Burke, D. J. Bradwell, K. Jiang, A. A. Tomaszowska, K. Wang, W. Wei, L. A. Ortiz, S. A. Barriga, S. M. Poizeau, and D. R. Sadoway, *Chem. Rev.* **113**, 2075 (2013).
- 6 D. H. Kelley and T. Weier, *Appl. Mech. Rev.* **70**, 020801 (2018).
- 7 G. I. L. van Oudenaren, J. A. Ocádiz-Flores, and A. L. Smith, *J. Mol. Liq.* **342**, 117470 (2021).
- 8 T. A. Utigard, K. Friesen, R. R. Roy, J. Lim, A. Silny, and C. Dupuis, *JOM* **50**, 38 (1998).
- 9 M. A. Williamson and J. L. Willit, *Nucl. Eng. Technol.* **43**, 329 (2011).
- 10 A. Merwin, M. A. Williamson, J. L. Willit, and D. Chidambaram, *J. Electrochem. Soc.* **164**, H5236 (2017).
- 11 X.-L. Xi, M. Feng, L.-W. Zhang, and Z.-R. Nie, *Int. J. Miner., Metall. Mater.* **27**, 1599 (2020).
- 12 M. J. L. Sangster and M. Dixon, *Adv. Phys.* **25**, 247 (1976).
- 13 M. Rovere and M. P. Tosi, *Rep. Prog. Phys.* **49**, 1001 (1986).
- 14 D. I. Page and K. Mika, *J. Phys. C: Solid State Phys.* **4**, 3034 (1971).
- 15 F. G. Edwards, J. E. Enderby, R. A. Howe, and D. I. Page, *J. Phys. C: Solid State Phys.* **8**, 3483 (1975).
- 16 S. Biggin and J. E. Enderby, *J. Phys. C: Solid State Phys.* **15**, L305 (1982).
- 17 S. Eisenberg, J.-F. Jal, J. Dupuy, P. Chieux, and W. Knoll, *Philos. Mag. A* **46**, 195 (1982).
- 18 M. Wilson and P. A. Madden, *J. Phys.: Condens. Matter* **5**, 2687 (1993).
- 19 P. A. Madden and M. Wilson, *Chem. Soc. Rev.* **25**, 339 (1996).
- 20 F. Hutchinson, A. J. Rowley, M. K. Walters, M. Wilson, P. A. Madden, J. C. Wasse, and P. S. Salmon, *J. Chem. Phys.* **111**, 2028 (1999).
- 21 M.-M. Walz, M. M. Ghahremanpour, P. J. van Maaren, and D. van der Spoel, *J. Chem. Theory Comput.* **14**, 5933 (2018).
- 22 M.-M. Walz and D. van der Spoel, *Phys. Chem. Chem. Phys.* **21**, 18516 (2019).
- 23 S. Tovey, A. N. Krishnamoorthy, G. Sivaraman, J. Guo, C. Benmore, A. Heuer, and C. Holm, *J. Phys. Chem. C* **124**, 25760 (2020).
- 24 R. J. F. Leote de Carvalho and R. Evans, *Mol. Phys.* **83**, 619 (1994).
- 25 P. Koblinski, J. Eggebrecht, D. Wolf, and S. R. Phillpot, *J. Chem. Phys.* **113**, 282 (2000).
- 26 M. A. Gebbie, H. A. Dobbs, M. Valtiner, and J. N. Israelachvili, *Proc. Natl. Acad. Sci. U. S. A.* **112**, 7432 (2015).
- 27 A. M. Smith, A. A. Lee, and S. Perkin, *J. Phys. Chem. Lett.* **7**, 2157 (2016).
- 28 M. A. Gebbie, A. M. Smith, H. A. Dobbs, A. A. Lee, G. G. Warr, X. Banquy, M. Valtiner, M. W. Rutland, J. N. Israelachvili, S. Perkin, and R. Atkin, *Chem. Commun.* **53**, 1214 (2017).

- ²⁹P. Cats, R. Evans, A. Härtel, and R. van Roij, *J. Chem. Phys.* **154**, 124504 (2021).
- ³⁰H. Ohno and K. Furukawa, *J. Chem. Soc., Faraday Trans. 1* **77**, 1981 (1981).
- ³¹S. Roy, F. Wu, H. Wang, A. S. Ivanov, S. Sharma, P. Halstenberg, S. K. Gill, A. M. Milinda Abeykoon, G. Kwon, M. Topsakal, B. Layne, K. Sasaki, Y. Zhang, S. M. Mahurin, S. Dai, C. J. Margulis, E. J. Maginn, and V. S. Bryantsev, *Phys. Chem. Chem. Phys.* **22**, 22900 (2020).
- ³²T. E. Faber and J. M. Ziman, *Philos. Mag.* **11**, 153 (1965).
- ³³A. B. Bhatia and D. E. Thornton, *Phys. Rev. B* **2**, 3004 (1970).
- ³⁴H. E. Fischer, A. C. Barnes, and P. S. Salmon, *Rep. Prog. Phys.* **69**, 233 (2006).
- ³⁵F. H. Stillinger, Jr. and R. Lovett, *J. Chem. Phys.* **49**, 1991 (1968).
- ³⁶P. S. Salmon, *J. Phys.: Condens. Matter* **18**, 11443 (2006).
- ³⁷N. H. March and M. P. Tosi, *Coulomb Liquids* (Academic Press, London, 1984).
- ³⁸J.-P. Hansen and I. P. McDonald, *Theory of Simple Liquids*, 3rd ed. (Elsevier, Amsterdam, 2006).
- ³⁹V. F. Sears, *Neutron News* **3**, 26 (1992).
- ⁴⁰H. E. Fischer, G. J. Cuello, P. Palteau, D. Feltin, A. C. Barnes, Y. S. Badyal, and J. M. Simonson, *Appl. Phys. A* **74**, S160 (2002).
- ⁴¹H. Bertagnolli, P. Chieux, and M. D. Zeidler, *Mol. Phys.* **32**, 759 (1976).
- ⁴²J. F. Jal, C. Mathieu, P. Chieux, and J. Dupuy, *Philos. Mag. B* **62**, 351 (1990).
- ⁴³A. Zeidler, "Ordering in amorphous binary systems," Ph.D. thesis, University of Bath, UK, 2009.
- ⁴⁴K. H. Stern, *Chem. Rev.* **66**, 355 (1966).
- ⁴⁵G. J. Janz, *Molten Salts Handbook* (Academic Press, New York, 1967).
- ⁴⁶P. S. Salmon, *J. Phys. F: Met. Phys.* **18**, 2345 (1988).
- ⁴⁷P. S. Salmon, S. Xin, and H. E. Fischer, *Phys. Rev. B* **58**, 6115 (1998).
- ⁴⁸G. J. Janz, *J. Phys. Chem. Ref. Data* **9**, 791 (1980).
- ⁴⁹E. R. Van Artsdalen and I. S. Yaffe, *J. Phys. Chem.* **59**, 118 (1955).
- ⁵⁰S. Kohara, M. Itou, K. Suzuya, Y. Inamura, Y. Sakurai, Y. Ohishi, and M. Takata, *J. Phys.: Condens. Matter* **19**, 506101 (2007).
- ⁵¹E. N. Maslen, A. G. Fox, and M. A. O'Keefe, in *International Tables for Crystallography*, edited by A. J. C. Wilson and E. Prince (Kluwer, Dordrecht, 1999), Vol. C, Chap. 6.1.1, p. 548.
- ⁵²D. T. Cromer and J. B. Mann, *J. Chem. Phys.* **47**, 1892 (1967).
- ⁵³D. T. Cromer, *J. Chem. Phys.* **50**, 4857 (1969).
- ⁵⁴K. F. Ludwig, Jr., W. K. Warburton, L. Wilson, and A. I. Bienenstock, *J. Chem. Phys.* **87**, 604 (1987).
- ⁵⁵A. Zeidler, P. S. Salmon, R. A. Martin, T. Usuki, P. E. Mason, G. J. Cuello, S. Kohara, and H. E. Fischer, *Phys. Rev. B* **82**, 104208 (2010).
- ⁵⁶M. Born and J. E. Mayer, *Z. Physik* **75**, 1 (1932).
- ⁵⁷A. J. Stone, *The Theory of Intermolecular Forces*, 2nd ed. (Oxford University Press, Oxford, 2013).
- ⁵⁸K. T. Tang and J. P. Toennies, *J. Chem. Phys.* **80**, 3726 (1984).
- ⁵⁹B. G. Dick, Jr. and A. W. Overhauser, *Phys. Rev.* **112**, 90 (1958).
- ⁶⁰D. Bedrov, J.-P. Piquemal, O. Borodin, A. D. MacKerell, Jr., B. Roux, and C. Schröder, *Chem. Rev.* **119**, 7940 (2019).
- ⁶¹A. Aguado, L. Bernasconi, S. Jahn, and P. A. Madden, *Faraday Discuss.* **124**, 171 (2003).
- ⁶²P. Jemmer, M. Wilson, P. A. Madden, and P. W. Fowler, *J. Chem. Phys.* **111**, 2038 (1999).
- ⁶³C. Domene, P. W. Fowler, M. Wilson, P. A. Madden, and R. J. Wheatley, *Chem. Phys. Lett.* **333**, 403 (2001).
- ⁶⁴C. Domene, P. W. Fowler, P. A. Madden, J. Xu, R. J. Wheatley, and M. Wilson, *J. Phys. Chem. A* **105**, 4136 (2001).
- ⁶⁵P. W. Fowler and P. A. Madden, *Phys. Rev. B* **31**, 5443 (1985).
- ⁶⁶N. Ohtori, M. Salanne, and P. A. Madden, *J. Chem. Phys.* **130**, 104507 (2009).
- ⁶⁷S. Nosé, *J. Chem. Phys.* **81**, 511 (1984).
- ⁶⁸W. G. Hoover, *Phys. Rev. A* **31**, 1695 (1985).
- ⁶⁹G. J. Martyna, D. J. Tobias, and M. L. Klein, *J. Chem. Phys.* **101**, 4177 (1994).
- ⁷⁰J. J. Salacuse, A. R. Denton, and P. A. Egelstaff, *Phys. Rev. E* **53**, 2382 (1996).
- ⁷¹A. Baumketner and Y. Chushak, *J. Non-Cryst. Solids* **250–252**, 354 (1999).
- ⁷²A. D. Kirshenbaum, J. A. Cahill, P. J. McGonigal, and A. V. Grosse, *J. Inorg. Nucl. Chem.* **24**, 1287 (1962).
- ⁷³B. Lorenz, H. Frei, and A. Jabs, *Z. Phys. Chem.* **61U**, 468 (1908).
- ⁷⁴F. M. Jaeger, *Z. Anorg. Allg. Chem.* **101**, 1 (1917).
- ⁷⁵K. Honda and H. Endo, *Z. Anorg. Allg. Chem.* **154**, 238 (1926).
- ⁷⁶F. Sauerwald, H. Allendorf, and P. Landschütz, *Z. Anorg. Allg. Chem.* **135**, 327 (1924).
- ⁷⁷K. Arndt and A. Gessler, *Z. Elektrochem.* **14**, 665 (1908).
- ⁷⁸E. Brunner, *Z. Anorg. Chem.* **38**, 350 (1904).
- ⁷⁹G. J. Janz, R. P. T. Tomkins, C. B. Allen, J. R. Downey, Jr., G. L. Garner, U. Krebs, and S. K. Singer, *J. Phys. Chem. Ref. Data* **4**, 871 (1975).
- ⁸⁰J. W. E. Lewis and K. Singer, *J. Chem. Soc., Faraday Trans. 2* **71**, 41 (1975).
- ⁸¹H. Ohno, K. Igarashi, N. Umesaki, and K. Furukawa, *X-ray Diffraction Analysis of Ionic Liquids*, Molten Salt Forum (Trans Tech Publications, Aedermannsdorf, 1994), Vol. 3.
- ⁸²P. S. Salmon, *Proc. R. Soc. London. A* **437**, 591 (1992).
- ⁸³P. S. Salmon and A. Zeidler, *J. Stat. Mech.: Theory Exp.* **2019**, 114006.
- ⁸⁴J. O. 'M. Bockris and N. E. Richards, *Proc. R. Soc. London. A* **241**, 44 (1957).
- ⁸⁵P. S. Salmon, *J. Phys.: Condens. Matter* **17**, S3537 (2005).
- ⁸⁶M. W. Chase, Jr., *NIST-JANAF Thermochemical Tables*, 4th ed., Journal of Physical and Chemical Reference Data, Monograph 9 (AIP & American Chemical Society, Woodbury, NY, 1998); available at <https://webbook.nist.gov/cgi/cbook.cgi?Source=1998CHA1-1951&Units=SI>.
- ⁸⁷P. S. Salmon and A. Zeidler, *Structure of Molten NaCl and the Decay of the Pair-Correlations* (University of Bath Research Data Archive, 2022).